NISSUNA UMANA INVESTIGAZIONE SI PUO DIMANDARE VERA SCIENZIA
S'ESSA NON PASSA PER LE MATEMATICHE DIMOSTRAZIONI
LEONARDO DA VINCI

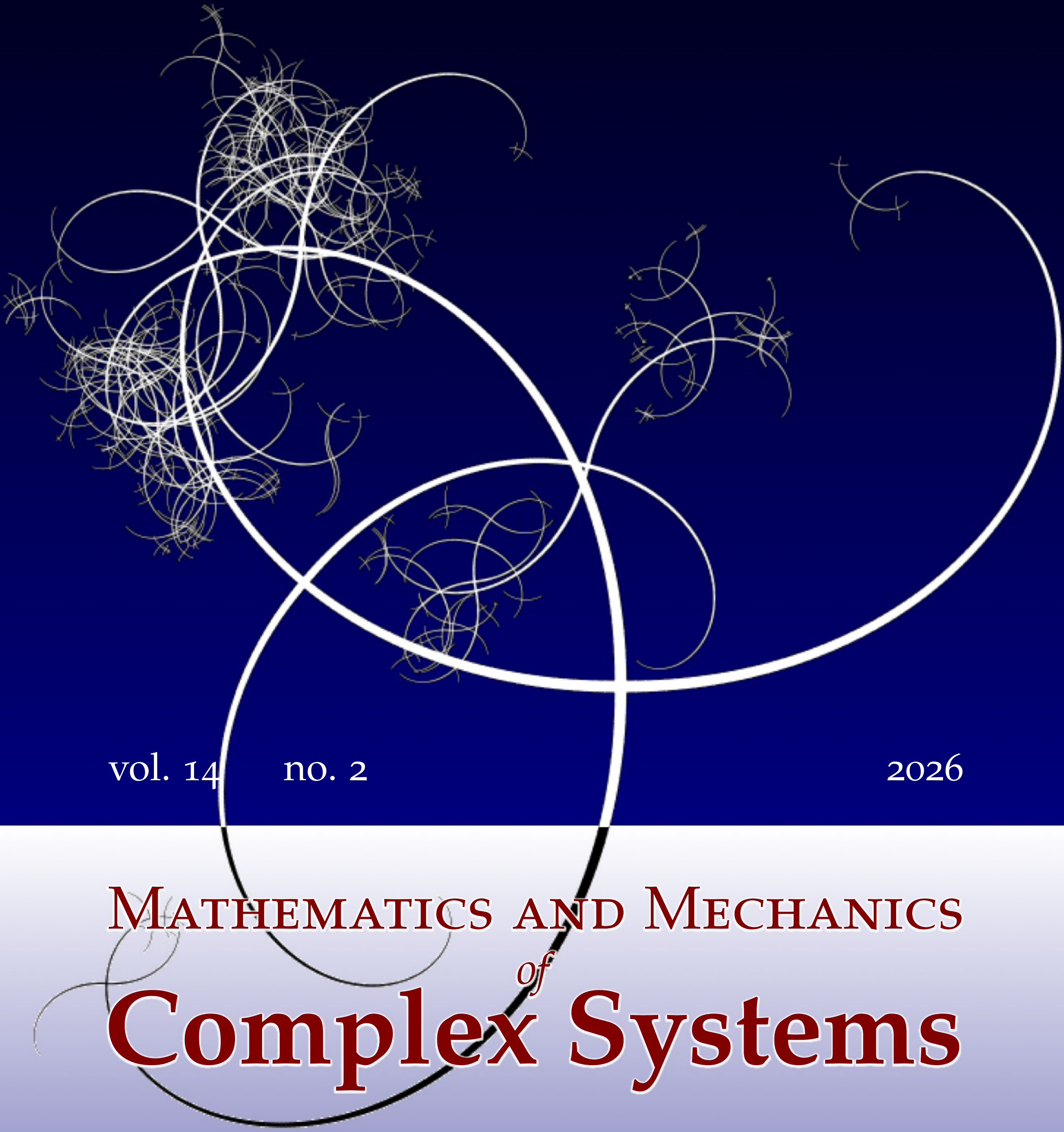

vol. 14 no. 2 2026

MATHEMATICS AND MECHANICS of Complex Systems

ANGELO SCROFANI, EMILIO BARCHIESI, BERNARDINO CHIAIA, ANIL MISRA AND LUCA PLACIDI

DIFFUSION OF A DAMAGING FLUID THROUGH A DAM-SHAPED BIDIMENSIONAL BODY FOR THE ESTIMATION OF ITS LIFETIME

MATHEMATICS AND MECHANICS OF COMPLEX SYSTEMS
Vol. 14 (2026), No. 2, pp. 117–142
DOI: 10.2140/memocs.2026.14.117

DIFFUSION OF A DAMAGING FLUID THROUGH A DAM-SHAPED BIDIMENSIONAL BODY FOR THE ESTIMATION OF ITS LIFETIME

ANGELO SCROFANI, EMILIO BARCHIESI, BERNARDINO CHIAIA, ANIL MISRA AND LUCA PLACIDI

The aging phenomena are often associated with the diffusion of certain particles which then activate internal chemical reactions. In this paper, the system of such particles is modelled with an damaging fluid and a hemi-variational method is proposed in order to describe damage and deformation of a dam-shaped two-dimensional body, where a key point is the introduction of the coupling between the damage and the damaging fluid concentration. Another important key point of the present model is the presence of energetic thresholds for damage activation, which are assumed to be different in tension (lower) and in compression (higher).

In this work, the body is subjected not only to the self-weight of the two-dimensional dam body and to the left-hand side water pressure, and therefore to the distributed external loads, dual of the displacement field, but also to the dual of the concentration of the mentioned damaging fluid, called the *external distributed damaging fluid influx pressure*. The parametric analyses are carried out in terms of diffusivity and damage-concentration coupling. The influx pressure drives the incoming flow of the damaging fluid, which is coupled with the damage variable, which is induced to evolve until the failure event, which characterises the lifetime of the structure. In order to evaluate the reasonableness of the model two cases are analysed: in the first one the body is modelled having a rectangular shape. In the second one a realistic trapezoidal dam shape is considered. Both have the same area and height in order to compare the results.

This comparison yields the following intuitive considerations. First of all, at the beginning of the time history, i.e., at the time at which the structure is assumed to be built, the tensile state, evaluated by the positive part of the trace of the deformation tensor, of the rectangular structure, is much higher then that of the trapezoidal one. The evolution of damage is faster in the rectangular model and, as expected, the present trapezoidal shapes for the design of the dams possess a longer lifetime and are valid not only for the structural response at the time of construction but also, within the presented model, for a better aging performance. It is worth noting that this is a standard result for dam engineers, and justifies the shapes that are used in the present dam design.

1. Introduction

1.1. ***Dam health monitoring.*** The monitoring [38; 53; 60; 69] of dams is a critical part of structural health monitoring, and as such, there has been continuous research efforts in investigating this issue [10; 47]. The mechanical integrity of dams may be affected by many phenomena: not only mechanical

---

Communicated by Francesco dell'Isola.
MSC2020: 65Nxx, 65Qxx, 74Gxx, 74Rxx, 76Sxx.
Keywords: dam, aging, fluid diffusion, damage, hemivariational, Rayleigh.

loads, but also the diffusion of particles, and the resulting chemical interactions. Indeed, the diffusion of particles may contribute to the nucleation and growth of microcracks inside the dam [17; 32; 48; 71], thus motivating research efforts to model such diffusive phenomena [8]. More specifically, various types of diffusing species may be involved, leading to different effects. For example, moisture content may activate damage through creeping [45; 76; 77]. Aging phenomena may be activated [59] by a damaging fluid spreading through the dam by capillary action. [5; 7; 52], or sorption of particles [45], resulting in chemical interactions between those aging elements and the dam material [14; 15; 21; 22; 23; 24; 65]. The initiation of damage can trigger a cascading effect, activating cracks [4; 11] whose propagation may lead to structural collapse [46; 50; 51; 58]. Such collapse, in the case of strategically important structures [79] like dams, can result in catastrophic events with severe consequences for human life.

1.2. ***Variational modelling approaches.*** The present work is a continuation of previous research efforts to model the deformation and aging-related damage of concrete dams. A one-dimensional shear deformable beam model, commonly employed in the literature [6; 19; 25; 37], has been proposed in [70], and it is now extended to a two-dimensional case in the present work. Our modelling approach lies within the framework of variational principles [29; 39], which are applied to the derivation of balance equations for generalised continuum models. They involve, in a nonclassical way, the kinematic quantities describing the strain of the continuum [30]. Among those generalised continua, higher-gradient continua have been studied and applied to model nonlocal elastic effects and they take into account the derivatives of the considered strain tensor in the deformation energy. As a consequence, such models are able to account for phenomena such as strain localisation, which cannot be correctly considered by classical Cauchy continua [20; 68]. Thus, strain-gradient continua have been used extensively for modelling metamaterials [16; 18], ie. synthetic materials specifically engineered to have exotic behaviours resulting from their microstructure [28; 31; 33]. They are also used here to avoid, e.g., mesh dependent strain localisation phenomenon

1.3. ***Outline.*** The physical-mathematical model is formulated in Section 2 as a 2D problem: the kinematic description is introduced, before defining energy functional to model the considered phenomenon, and then a hemi-variational inequality principle is used to formulate the mathematical problem. Then, numerical investigations are carried out and presented in Section 3 for dams having various cross sections. Finally, the work done and main results are summarised in Section 4 as a conclusion.

2. Formulation of the 2D problem

2.1. ***Preliminary definitions.*** The dam is modelled as a 2-D continuum body $\mathcal{B}$. Its points are characterised by means of the coordinates $\boldsymbol{X} = X_i \hat{\boldsymbol{e}}_i$ (where $\|\hat{\boldsymbol{e}}_i\| = 1$ and $i = 1, 2$) in a given reference configuration. The set of the kinematical descriptors which depend upon $\boldsymbol{X}$ and t is composed of (i) the horizontal displacement $u_1(\boldsymbol{X}, t)$, (ii) the vertical displacement $u_2(\boldsymbol{X}, t)$, (iii) the concentration of a fluid $c(\boldsymbol{X}, t)$ and (iv) the damage $\omega(\boldsymbol{X}, t)$. The damage, whose evolution is supposed driven by the concentration of the damaging fluid c, is a no-decreasing in time irreversible field and it is represented by means of a scalar variable ω ranging from 0 (denoting the undamaged state) to 1 (denoting the attainment of the failure). Let $\boldsymbol{u} = \boldsymbol{u}(\boldsymbol{X}, t) = u_i \hat{\boldsymbol{e}}_i$ (where $\|\hat{\boldsymbol{e}}_i\| = 1$ and $i = 1, 2$) be the displacement vector, $\boldsymbol{\Phi}(\boldsymbol{X}, t)$ is the placement function, $\mathbb{F}$ is the deformation gradient tensor and $\mathbb{G}$ is the Green strain tensor. Indicating with $\boldsymbol{x} = x_i \hat{\boldsymbol{e}}_i$ the coordinates, in the current configuration, of the point having coordinates $\boldsymbol{X}$ in the reference configuration, one has

$$\boldsymbol{x} = \boldsymbol{\Phi}(\boldsymbol{X}, t) = \boldsymbol{X} + \boldsymbol{u}, \quad \mathbb{F} = \nabla \boldsymbol{\Phi}, \quad \mathbb{G} = \tfrac{1}{2}(\mathbb{F}^T \mathbb{F} - \mathbb{I}) \tag{1}$$

or, in index notation,

$$x_i = \Phi_i = X_i + u_i, \quad F_{ij} = \frac{\partial \Phi_i}{\partial X_j} = u_{i,j} + \delta_{ij}, \quad G_{ij} = \tfrac{1}{2}(F_{ki} F_{kj} - \delta_{ij}) \tag{2}$$

where

$$u_{i,j} = \frac{\partial u_i}{\partial X_j} \tag{3}$$

and δ_{ij} is the Kronecker delta. Thus, from (2) and (3), in terms of the displacement $\boldsymbol{u}$ the Green strain tensor is

$$G_{ij} = \tfrac{1}{2}(u_{i,j} + u_{j,i} + u_{h,i} u_{h,j}). \tag{4}$$

2.2. ***Total deformation energy functional.*** From [62; 70; 78] the energy functional can be split into three parts.

(i) The elastic part,

$$\mathcal{E}_e(u, \omega) = \int_{\mathcal{B}} \big[U(\mathbb{G}, \nabla\mathbb{G}, \omega) - \boldsymbol{b}^{\text{ext}} \cdot \boldsymbol{u} - \mathbb{M}^{\text{ext}} : \nabla \boldsymbol{u}\big]\, dA - \int_{\partial\mathcal{B}} \big[\boldsymbol{t}^{\text{ext}} \cdot \boldsymbol{u} + \boldsymbol{\tau}^{\text{ext}} \cdot [(\nabla \boldsymbol{u})\boldsymbol{n}]\big]\, ds - \int_{\partial\partial\mathcal{B}} \boldsymbol{f}^{\text{ext}} \cdot \boldsymbol{u}, \tag{5}$$

where U is the internal deformation energy density, $\boldsymbol{b}^{\text{ext}}$ is the external body force (i.e., per unit area), $\mathbb{M}^{\text{ext}}$ is the external body double force (i.e., per unit area), ":" represents the scalar product between second-order tensors, so that

$$\mathbb{M}^{\text{ext}} : \nabla \boldsymbol{u} = M_{ij}^{\text{ext}} u_{i,j}, \tag{6}$$

$\boldsymbol{t}^{\text{ext}}$ and $\boldsymbol{\tau}^{\text{ext}}$ are, respectively, the external force and double force per unit length acting on the boundary $\partial\mathcal{B}$ of the domain, and $\boldsymbol{n}$ is the unit normal. The vector $\boldsymbol{f}^{\text{ext}}$ is the concentrated external force applied on the vertices, which is the boundary of the boundary denoted as $\partial\partial\mathcal{B}$.

(ii) The diffusion part,

$$\mathcal{E}_c(c) = \int_{\mathcal{B}} \big[\tfrac{1}{2} K^{\text{DIF}} \|\nabla c\|^2 + \tfrac{1}{2} K_F c^2\big]\, dA - \int_{\partial\mathcal{B}} [b_c^{\text{ext}} c]\, ds, \tag{7}$$

where K^{DIF}, K_F and b_c^{ext} are the diffusion coefficient of the damaging fluid through the matrix, the fluid elasticity and the external distributed aging influx pressure, respectively.

(iii) The rate-independent dissipative part,

$$\mathcal{E}_\omega(c,\omega)=\int_{\mathcal{B}}\big[K_{\omega 0}\omega+K_{c\omega}c\omega+\tfrac{1}{2}K_\omega\omega^2\big]\,dA, \tag{8}$$

where $K_{\omega 0}$, $K_{c\omega}$ and K_ω represent the damage yielding point, the concentration-damage coupling factor and the resistance to damage (or damage inertia). The yielding point $K_{\omega 0}$ is assumed to be different in tension and in compression and therefore it depends upon the Heaviside function $H(\,\cdot\,)$ of the trace of the Green deformation tensor $\operatorname{tr}(\mathbb{G})$,

$$K_{\omega 0}=\bar{K}_{\omega 0}[1+(\xi-1)H(-\operatorname{tr}\mathbb{G}),\,] \tag{9}$$

where $\bar{K}_{\omega 0}$ is the damage yielding point in tension and ξ is the amplification factor that increases the value of $K_{\omega 0}$ in compression, so that

$$K_{\omega 0}=\begin{cases}\bar{K}_{\omega 0} & \text{in tension, } \operatorname{tr}G>0,\\ \xi\bar{K}_{\omega 0} & \text{in compression, } \operatorname{tr}G<0.\end{cases} \tag{10}$$

The energy functional $\mathcal{E}$ is assumed to be additively decomposed in the parts given in (5), (7) and (8):

$$\begin{aligned}\mathcal{E}(u,c,\omega)&=\mathcal{E}_e(u,\omega)+\mathcal{E}_c(c)+\mathcal{E}_\omega(c,\omega)\\ &=\int_{\mathcal{B}}[U_e(\mathbb{G},\nabla\mathbb{G},\omega)-\boldsymbol{b}^{\text{ext}}\cdot\boldsymbol{u}-\mathbb{M}^{\text{ext}}:\nabla\boldsymbol{u}]\,dA+\int_{\mathcal{B}}\big[\tfrac{1}{2}K^{\text{DIF}}\|\nabla c\|^2+\tfrac{1}{2}K_F(c)^2\big]\,dA\\ &\quad-\int_{\partial\mathcal{B}}\big[\boldsymbol{t}^{\text{ext}}\cdot\boldsymbol{u}+\boldsymbol{\tau}^{\text{ext}}\cdot[(\nabla\boldsymbol{u})\boldsymbol{n}]\big]\,ds-\int_{\partial\mathcal{B}}[\mathbf{b_c}^{\text{ext}}c]\,ds-\int_{\partial\partial\mathcal{B}}\boldsymbol{f}^{\text{ext}}\cdot\boldsymbol{u}\\ &\quad+\int_{\mathcal{B}}\big[K_{\omega 0}\omega+K_{c\omega}c\omega+\tfrac{1}{2}K_\omega\omega^2\big]\,dA.\end{aligned} \tag{11}$$

and its variation, in index notation, is

$$\begin{aligned}&\delta\mathcal{E}(u,c,\omega)\\ &\quad=\delta\mathcal{E}_e(u,\omega)+\delta\mathcal{E}_c(c)+\delta\mathcal{E}_\omega(c,\omega)\\ &\quad=-\int_{\mathcal{B}}\big[(\sigma_{ij,j}-T_{ijh,hj}+b_i^{\text{ext}}-M_{ij,j}^{\text{ext}})\delta u_i\big]\,dA-\int_{\mathcal{B}}\big[(K^{\text{DIF}}c_{,i}c_{,i}+K_Fc+K_{c\omega}\omega)\delta c\big]\,dA\\ &\qquad+\int_{\partial\mathcal{B}}\big[(t_i-t_i^{\text{ext}}-m_{ij}^{\text{ext}}n_j)\delta u_i\big]\,ds+\int_{\partial\mathcal{B}}\big[(\tau_i-\tau_i^{\text{ext}})n_k\delta u_{i,k}\big]\,ds+\int_{\partial\mathcal{B}}\big[(K^{\text{DIF}}c_{,i}n_j-b_c^{\text{ext}})\delta c\big]\,ds\\ &\qquad+\int_{\partial\partial\mathcal{B}}[f_i-f_i^{\text{ext}}]\delta u_i+\int_{\mathcal{B}}\Big[\Big(\frac{\partial U_e}{\partial\omega}+K_{\omega 0}+K_{c\omega}c+K_\omega\omega\Big)\delta\omega\Big]\,dA,\end{aligned} \tag{12}$$

where the stress σ_{ij} and hyperstress T_{ijh} are

$$\sigma_{ij}=\frac{\partial U}{\partial G_{ij}}=\frac{\partial U}{\partial G_{ji}}=\sigma_{ji}\quad\text{and}\quad T_{ijh}=\frac{\partial U}{\partial G_{ij,h}}=\frac{\partial U}{\partial G_{ji,h}}=T_{jih}, \tag{13}$$

and the internal stress, double stress and vertex stress vectors are respectively

$$t_i=[\sigma_{ij}-T_{ijh,h}]n_j-(T_{ijh}n_hP_{jk})_{,l}P_{jl},\qquad \tau_i=T_{ijh}n_hn_j,\qquad f_i=T_{ijh}V_{hj}. \tag{14}$$

Here, as in [62], $P_{ij} = \delta_{ij} - n_i n_j$ is the tangential projector operator, $V_{hj} = n^l_h v^l_j + n^r_h v^r_j$ is the vertex operator and v_j is the external tangent unit vector. Superscript l and r refer to the *left* and *right* side of a vertex-point to which a concentrated force is applied. As already pointed out, the damage ω is defined by a nondecreasing in time real variable, that is, we assume

$$\frac{\partial \omega}{\partial t} \geq 0 \quad \forall \boldsymbol{X} \in \mathcal{B}. \tag{15}$$

The Rayleigh functional, which in this work is linked only with the rate of fluid concentration, is assumed to be a quadratic form of the velocity:

$$\mathcal{R}(\dot{c}) = \int_{\mathcal{B}} \left[\tfrac{1}{2} c_c \dot{c}^2\right] dA, \tag{16}$$

where c_c is the damping coefficient. Its variation and increment are indicated by $\tilde{\delta}$ and $\tilde{\Delta}$:

$$\tilde{\delta}\mathcal{R}(\dot{c}, \delta c) = \int_{\mathcal{B}} [c_c \dot{c}\, \delta c]\, dA \quad \tilde{\Delta}\mathcal{R}(\dot{c}, \Delta c) = \int_{\mathcal{B}} [c_c \dot{c}\, \Delta c]\, dA \tag{17}$$

We further introduce the symbol

$$\Lambda = (u_1, u_2, c, \omega) \tag{18}$$

for the set of the kinematical descriptors, and its variation and increment

$$\delta\Lambda = (\delta u_1, \delta u_2, \delta c, \delta\omega), \quad \Delta\Lambda = (\Delta u_1, \Delta u_2, \Delta c, \Delta\omega). \tag{19}$$

It follows, trivially, that

$$\Lambda + \delta\Lambda = (u_1 + \delta u_1, u_2 + \delta u_2, c + \delta c,\ \omega + \delta\omega), \tag{20}$$

$$\Lambda + \Delta\Lambda = (u_1 + \Delta u_1, u_2 + \Delta u_2, c + \Delta c,\ \omega + \Delta\omega). \tag{21}$$

As in [70] the condition (15) implies the necessity of a generalisation of the standard variational principle in the so-called hemivariational principle.

2.3. ***Hemivariational inequality principle.*** As in [61], a monotonically increasing time sequence $T_i \in \{T_i\}_{i=0}^n$ with $T_i \in \mathbb{R}$ and $n \in \mathbb{N}$ is introduced, considering an initial and trivial datum (at $t_0 = T_0$) for each of the fundamental kinematical quantities. Let us consider the set of kinematically admissible placements and the kinematically admissible variations of the placements. Noting, from (15), that the admissible variation of the irreversible kinematic quantity ω must not be negative, we have

$$\delta\omega \geq 0. \tag{22}$$

Now, the first variation of the energy functional is calculated as

$$\delta\mathcal{E}(\Lambda, \delta\Lambda) = \mathcal{E}(\Lambda + \delta\Lambda) - \mathcal{E}(\Lambda), \tag{23}$$

where the terms of order 2 or higher can be neglected. Let us consider that, at the i-th instant T_i, the increment of the fundamental kinematic quantities is calculated by the difference between these quantities as evaluated at the times T_i and T_{i-1}, namely,

$$\Delta\Lambda = (\Lambda)_{T_i} - (\Lambda)_{T_{i-1}}, \tag{24}$$

and the increment of the energy functional has the consequent definition

$$\Delta\mathcal{E}(\Lambda, \Delta\Lambda) = \mathcal{E}(\Lambda + \Delta\Lambda) - \mathcal{E}(\Lambda). \tag{25}$$

As in (23) the terms of order 2 or higher can be neglected. In order to get governing equations for this newly introduced model, we assume that the motion $u_1(\boldsymbol{X}, t)$, $u_2(\boldsymbol{X}, t)$, $c(\boldsymbol{X}, t)$ and $\omega(\boldsymbol{X}, t)$ satisfies the hemivariational principle

$$\Delta\mathcal{E}(\Lambda, \Delta\Lambda) + \tilde{\Delta}\mathcal{R}(\dot{c}, \Delta c) \leq \delta\mathcal{E}(\Lambda, \delta\Lambda) + \tilde{\delta}\mathcal{R}(\dot{c}, \delta c) \tag{26}$$

for any admissible variation $\delta\Lambda$ of the fundamental kinematic quantities. Starting from (12), the variational principle implies the Euler–Lagrange equations of different type: a system of partial differential equations (for $i = 1, 2$) for the equilibrium

$$\sigma_{ij,j} - T_{ijh,hj} + b_i^{\text{ext}} - M_{ij,j}^{\text{ext}} = 0, \tag{27}$$

a differential equation for the diffusion

$$K^{\text{DIF}} c_{,i} c_{,i} + K_F c + K_{c\omega}\omega = c_c \dot{c}, \tag{28}$$

and the following set of boundary conditions:

$$\begin{aligned}
[t_i - t_i^{\text{ext}} - M_{ij}^{\text{ext}} n_j]\delta u_i &= 0 \quad \forall \boldsymbol{X} \in \partial\mathcal{B}, &(29)\\
(\tau_i - \tau_i^{\text{ext}})\delta u_{i,k} n_k &= 0 \quad \forall \boldsymbol{X} \in \partial\mathcal{B}, &(30)\\
[K^{\text{DIF}} c_{,i} n_i - b_c^{\text{ext}}]\delta c &= 0 \quad \forall \boldsymbol{X} \in \partial\mathcal{B}, &(31)\\
[f_i - f_i^{\text{ext}}]\delta u_i &= 0 \quad \forall \boldsymbol{X} \in \partial\partial\mathcal{B}. &(32)
\end{aligned}$$

The term K^{DIF}/c_c has the role of the diffusion coefficient for the classical diffusion equation, which is nevertheless modified by the fluid elasticity K_F and the concentration-damage coupling factor $K_{c\omega}$.

2.4. ***2D isotropic quadratic internal deformation energy density functional.*** The elastic part of the internal deformation energy density functional U_e of an isotropic second gradient material is (see [55])

$$\begin{aligned}
U_e(\mathbb{G}, \nabla\mathbb{G}, \omega) = \tfrac{1}{2}\lambda G_{ii} G_{jj} + \mu G_{ij} G_{ji} + 4\alpha_1 G_{ii,j} G_{jh,h} + \alpha_2 G_{ii,j} G_{kk,j}&\\
+ 4\alpha_3 G_{ij,i} G_{kj,k} + 2\alpha_4 G_{ij,k} G_{ij,k} + 4\alpha_5 G_{ij,k} G_{ik,j},& \quad (33)
\end{aligned}$$

where $\lambda, \mu, \alpha_i \in \mathbb{R}$ are parameters defined by

$$\lambda = (1-\omega)\lambda_0, \quad \mu = (1-\omega)\mu_0, \quad \alpha_i = (1+n\omega)\alpha_i^0, \quad \text{for } n \in [-1, +\infty),\ i \in \{1, 2, 3, 4, 5\}. \tag{34}$$

The parameters λ_0 and μ_0 are the Lamé constants, while the coefficients α_i^0 are the Mindlin parameters, related to the characteristic length and the Lamé constants [9] by

$$\alpha_1^0 = \alpha_2^0 = \tfrac{1}{112} L^2 \lambda_0, \quad \alpha_3^0 = \alpha_5^0 = \tfrac{1}{1120} L^2 (7\mu_0 + 3\lambda_0), \quad \alpha_4^0 = \tfrac{1}{1120} L^2 (7\mu_0 - 4\lambda_0). \tag{35}$$

Both the stiffnesses and the Mindlin parameters are affected by the damage ω, as shown in (34). An increase in ω reduces the contribution of the stiffnesses to the overall resistance and influences the coefficients α_i through the parameter n. As in [62], n is a weighting factor, ranging from -1 to ∞, through which the second-gradient terms associated with Mindlin's constants α_i contribute more or less significantly to the energy; see (33) and (36). For $n = -1$, when failure is reached ($\omega = 1$) the second-gradient terms related to the Mindlin coefficients α_i make no energy contribution. For $n = 0$ the coefficients α_i do not depend upon on the damage ω. Finally, for $n > 0$ the contribution of the second-gradient terms is present also in the cracked region, where $\omega = 1$.

Aging has different consequences. One is an increase in the damage ω (39), which reduces the Lamé parameters (34). In regions where damage has its maximum value $\omega = 1$, this effect is fully realised. By explicitly expressing the indices, (33) becomes

$$\begin{aligned} U_e(\mathbb{G}, \nabla\mathbb{G}, \omega) = {} & \big(\tfrac{1}{2}\lambda + \mu\big)(G_{11}^2 + G_{22}^2) + \lambda G_{11} G_{22} + 2\mu G_{12}^2 \\ & + (G_{11,1}^2 + G_{22,2}^2)(4\alpha_1 + \alpha_2 + 4\alpha_3 + 2\alpha_4 + 4\alpha_5) + (G_{11,1} G_{12,2} + G_{12,1} G_{22,2})(4\alpha_1 + 8\alpha_3) \\ & + (G_{11,2} G_{12,1} + G_{12,2} G_{22,1})(4\alpha_1 + 8\alpha_5) + (G_{11,2} G_{22,2} + G_{11,1} G_{22,1})(4\alpha_1 + 2\alpha_2) \\ & + (G_{11,2}^2 + G_{22,1}^2)(\alpha_2 + 2\alpha_4) + (G_{12,1}^2 + G_{12,2}^2)(4\alpha_3 + 4\alpha_4 + 4\alpha_5). \end{aligned} \tag{36}$$

If only the self-weight of the body $\mathcal{B}$, the pressure of the water p and the external distributed aging influx pressure b_c^{ext} act on the body, and replacing the internal deformation energy evaluated in (36), the internal energy functional (11) becomes

$$\begin{aligned} \mathcal{E} = {} & \int_{\mathcal{B}} \big[\big(\tfrac{1}{2}\lambda + \mu\big)(G_{11}^2 + G_{22}^2) + \lambda G_{11} G_{22} + 2\mu G_{12}^2\big]\, dA \\ & + \int_{\mathcal{B}} \big[(G_{11,1}^2 + G_{22,2}^2)(4\alpha_1 + \alpha_2 + 4\alpha_3 + 2\alpha_4 + 4\alpha_5)\big]\, dA \\ & + \int_{\mathcal{B}} \big[(G_{11,1} G_{12,2} + G_{12,1} G_{22,2})(4\alpha_1 + 8\alpha_3)\big]\, dA \\ & + \int_{\mathcal{B}} \big[(G_{11,2} G_{12,1} + G_{12,2} G_{22,1})(4\alpha_1 + 8\alpha_5)\big]\, dA \\ & + \int_{\mathcal{B}} \big[(G_{11,2} G_{22,2} + G_{11,1} G_{22,1})(4\alpha_1 + 2\alpha_2)\big]\, dA \\ & + \int_{\mathcal{B}} \big[(G_{11,2}^2 + G_{22,1}^2)(\alpha_2 + 2\alpha_4)\big]\, dA + \int_{\mathcal{B}} \big[(G_{12,1}^2 + G_{12,2}^2)(4\alpha_3 + 4\alpha_4 + 4\alpha_5)\big]\, dA \\ & + \int_{\mathcal{B}} \big[\tfrac{1}{2} K^{\text{DIF}} \|\nabla c\|^2 + \tfrac{1}{2} K_F c^2\big]\, dA + \int_{\mathcal{B}} \big[K_{\omega 0}\omega + K_{c\omega} c\omega + \tfrac{1}{2} K_\omega \omega^2\big]\, dA \\ & - \int_{\mathcal{B}} [\rho g u_2]\, dA - \int_{\partial\mathcal{B}} [p(\boldsymbol{u} \cdot \boldsymbol{n}) + b_c^{\text{ext}} c]\, ds, \end{aligned} \tag{37}$$

where ρ and g are the density of the body $\mathcal{B}$ and the acceleration of gravity. From the Karush–Kuhn–Tucker condition and (15) it follows that

$$(\omega - \tilde{\omega})\dot{\omega} = 0, \tag{38}$$

where $\tilde{\omega}$ is a tentative damage value, that is, an energy threshold above which the damage ω increases; its expression is

$$\begin{aligned}\tilde{\omega}\,(X,t) = K_{\omega}^{-1}\Big\{&\big(\tfrac{1}{2}\lambda_0+\mu_0\big)(G_{11}^2+G_{22}^2)+\lambda_0 G_{11}G_{22}+2\mu_0 G_{12}^2\\ &-n\big[(G_{11,1}^2+G_{22,2}^2)(4\alpha_1^0+\alpha_2^0+4\alpha_3^0+2\alpha_4^0+4\alpha_5^0)\\ &\qquad+(G_{11,1}G_{12,2}+G_{12,1}G_{22,2})(4\alpha_1^0+8\alpha_3^0)\\ &\qquad+(G_{11,2}G_{12,1}+G_{12,2}G_{22,1})(4\alpha_1^0+8\alpha_5^0)\\ &\qquad+(G_{11,2}G_{22,2}+G_{11,1}G_{22,1})(4\alpha_1^0+2\alpha_2^0)\\ &\qquad+(G_{11,2}^2+G_{22,1}^2)(\alpha_2^0+2\alpha_4^0)+(G_{12,1}^2+G_{12,2}^2)(4\alpha_3^0+4\alpha_4^0+4\alpha_5^0)\big]\\ &-(K_{\omega_0}+K_{c\omega}c)\Big\}\end{aligned} \tag{39}$$

For the concentration c to increase damage ω by lowering its threshold $K_{\omega 0}$ over time, the condition

$$K_{c\omega} < 0 \tag{40}$$

must hold. Clearly in order to obtain the unilateral behaviour of ω, numerically, the following condition is imposed:

$$\dot{\omega} < 0 \Longrightarrow \dot{\omega} = 0; \tag{41}$$

or, equivalently,

$$\tilde{\omega}\,(\boldsymbol{X}, T_i) < \omega\,(\boldsymbol{X}, T_{i-1}) \Longrightarrow \tilde{\omega}\,(\boldsymbol{X}, T_i) = \omega\,(\boldsymbol{X}, T_{i-1})\,. \tag{42}$$

3. Numerical investigation

In the following numerical treatment of a dam model, two cases are considered for the shape of the body $\mathcal{B}$ representing the dam: first a rectangle, then a crested trapezoid imitating the cross section of a realistic gravity dam (Figure 1). The area is the same in both models: $A_{\text{rect}} = A_{\text{trap}}$. The water is on the left. The mass density of the dam $\mathcal{B}$ is denoted by ρ_c, the water pressure by p_w, the height of $\mathcal{B}$ by H, and the height of the crest of the trapezoidal dam by h. We assume that the water reaches the top of the dam, so its height is also H.

It is assumed that the damaging fluid seeps into the structure from the left and that the distribution of the external influx pressure, b_c^{ext}, obeys a triangular law at the boundary, since it is proportional to the water pressure; thus,

$$b_c^{\text{ext}}(X_2) = \bar{b}_c^{\text{ext}}\,\frac{H - X_2}{H}, \tag{43}$$

where the constant $\bar{b}_c^{\text{ext}}$ is the maximum value attained by b_c^{ext}, occurring at the bottom of the interface, which we take as the coordinate origin, $X_1 = X_2 = 0$.

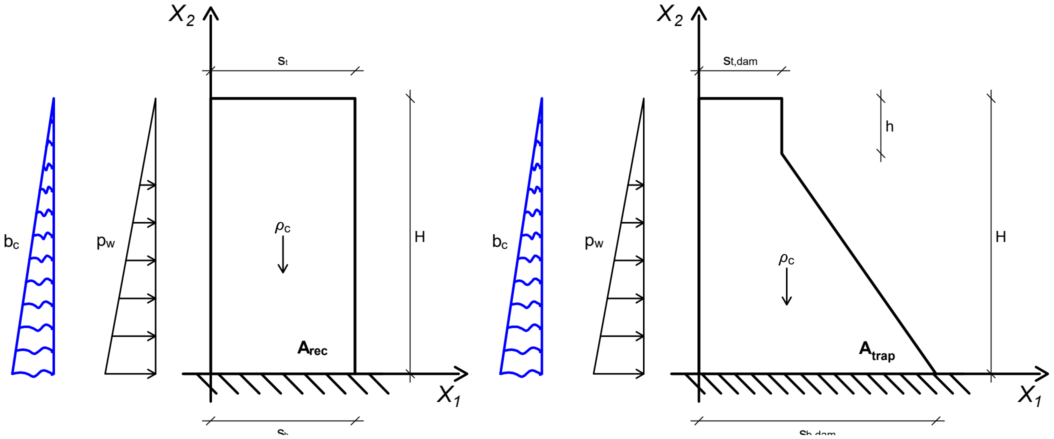

Figure 1. Model and boundary conditions for the two dam shapes: rectangular and trapezoidal.

$H = 10\,\mathrm{m}$
$s_t = 5.24\,\mathrm{m}$
$s_b = 5.24\,\mathrm{m}$
$s_{t,dam} = 3\,\mathrm{m}$
$s_{b,dam} = 8.6\,\mathrm{m}$
$h = 2\,\mathrm{m}$
$E = 4 \cdot 10^{10}\,\mathrm{N/m}$

$\lambda_0 = 1.11 \cdot 10^{10}\mathrm{N/m}$
$\mu_0 = 1.67 \cdot 10^{10}\mathrm{N/m}$
$\nu = 0.2$
$\xi = 10$
$\bar{b}_c^{\mathrm{ext}} = 10^{12}\mathrm{m}^2/\mathrm{s}^2$
$c_c = 10^{20}\mathrm{m}^5/\mathrm{kg} \cdot \mathrm{s}$
$n = 0$

$K_F = 10^{10}\,\mathrm{m}^4/\mathrm{kg} \cdot \mathrm{s}^2$
$K_{c\omega} = -5\,\mathrm{m}^2/\mathrm{s}^2$
$\bar{K}_{\omega 0} = 4\,\mathrm{N/m}$
$K_\omega = 30\,\mathrm{N/m}$
$K^{\mathrm{DIF}} = 10^{11}\,\mathrm{m}^6/\mathrm{kg} \cdot \mathrm{s}^2$
$\gamma_w = 10\,\mathrm{kN/m}^3$
$\gamma_c = 25\,\mathrm{kN/m}^3$

Table 1. Base parameter values for numerical investigations.

The analysis was carried out using the COMSOL Multiphysics software by an implicit method (generalised alpha method). Table 1 presents the parameters used for the calculations. Furthermore, the analyses include a damage check. Specifically, the analysis is terminated when the damage variable ω reaches its maximum value of 1 over a certain percentage of the total area, set at 1% in this case.

3.1. ***The rectangular case.*** The domain, as shown in Figure 2, is divided into two subdomains to apply

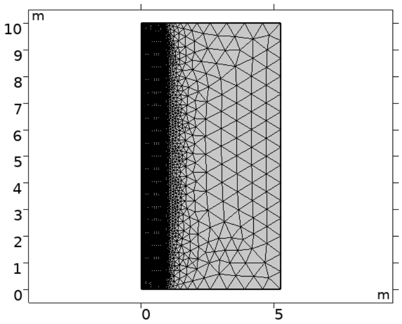

Figure 2. Most of the rectangular domain is discretised into elements of side length up to 67 cm, while a strip on the left is further refined with elements of maximum side length 5 cm.

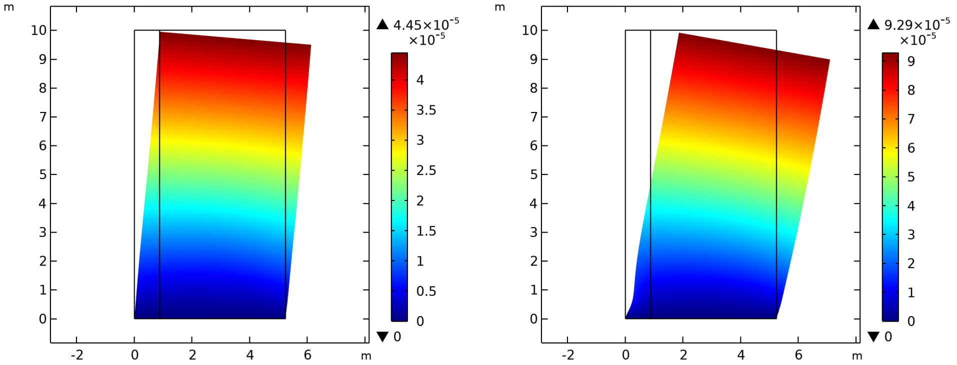

Figure 3. Colour plot of the horizontal displacement u_1 [m] in the deformed configuration. Left: initial time; right: final time $t \approx 88$ years. A multiplication factor of 20000 was applied to enhance the visibility of horizontal displacement.

a refined mesh only in a targeted region, to reduce computational costs. We expected a finer mesh is needed on the left side of the body, where diffusion and the rate of damage evolution are higher.

Initially, the displacements are mainly affected by the pressure of the water, as shown in Figure 3, left. They increase as in a cantilever beam model (Figure 3, right) when the stiffness decreases because the material becomes softer in the region where the damage is concentrated. When the damage parameter ω attains the value 1, the material in that region is considered completely failed with no load-bearing capacity. Consequently, the effective load-carrying cross-sectional area of the base of the body $\mathcal{B}$ decreases as the damage variable ω increases. In this numerical example, a constraint was imposed on the evolution of ω. The maximum allowable damaged area is set to 1% of the total area. By fixing a higher value for the percentage of the damaged area, we would observe greater final displacements.

The cantilever behaviour is also recognisable in Figure 4, where vertical displacements are shown. Specifically, positive and negative displacement values can be observed on the left and right boundaries, respectively. This indicates that the domain undergoes bending to the right, which corresponds to the direction of the external forces acting on the body $\mathcal{B}$.

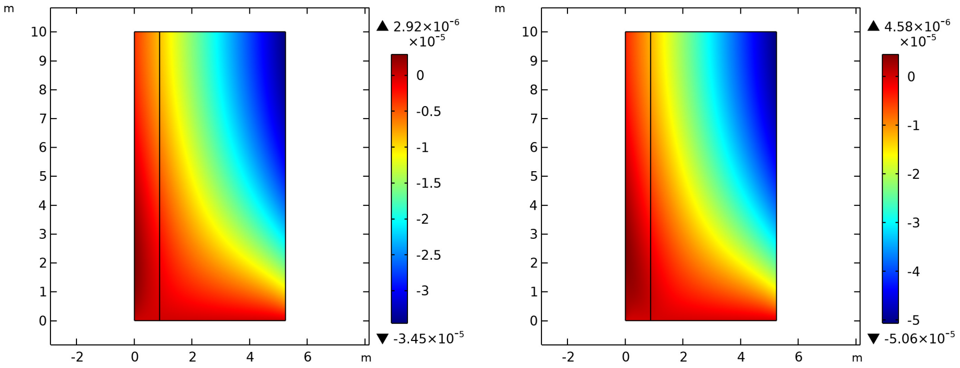

Figure 4. Colour plot of the vertical displacement u_2 [m]. Left: initial time; right: final time $t \approx 88$ years.

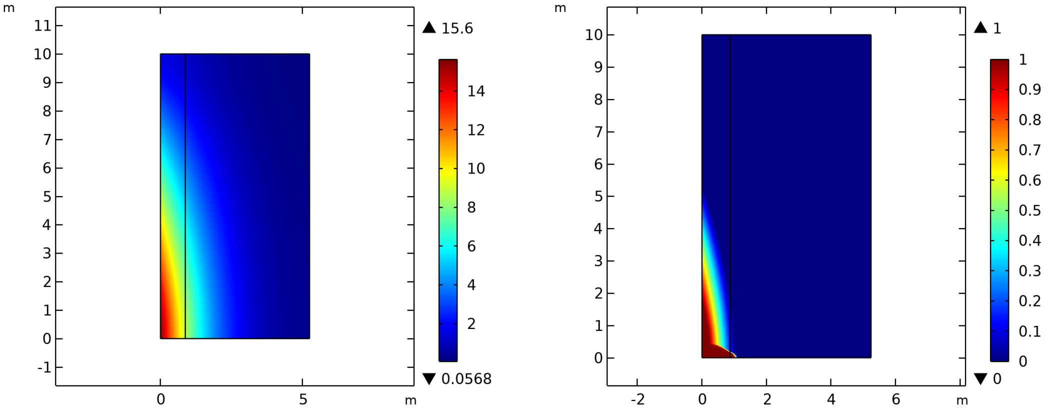

Figure 5. Colour plots at the final time $t \approx 88$ years. Left: concentration $c[\mathrm{kg/m^2}]$; right: damage ω.

As in [70], the concentration c and the damage ω evolve in a similar way, see Figure 5. The reason is the presence of the concentration-damage coupling factor $K_{c\omega}$ in (39) and the Karush–Kuhn–Tucker condition (41) or (42). Upon examination of Figure 5, right, a notably extensive distribution of damage at the base of the domain is observed. This phenomenon can be readily understood by considering not only the coupling between the damage induced by fluid diffusion and that resulting from external loads (which, albeit constant, act on a progressively diminishing resistant region at the base as consequence of reducing of the stiffnesses), but also the differing stress state that imposes a lower damage threshold (refer to (10) in which the damage yielding point $K_{\omega 0}$ is linked with the trace of the strain tensor $\mathbb{G}$). The area proximate to the lower-left corner is subjected to a positive trace of $\mathbb{G}$, therefore $K_{\omega 0}$ is 10 times less than in the region where it is in compressive state ($\xi = 10$ in Table 1).

To clarify the distribution of concentration c and damage ω we show in Figure 6 the evolution of these descriptors at a section with coordinate $X_2 = 0.5\mathrm{m}$ (the red line on the rectangular models in Figure 6).

Several analyses are conducted in Sections. 3.1.1 and 3.1.2 for different values of the diffusion coefficient K^{DIF} and the concentration-damage coupling factor $K_{c\omega}$, to highlight their role.

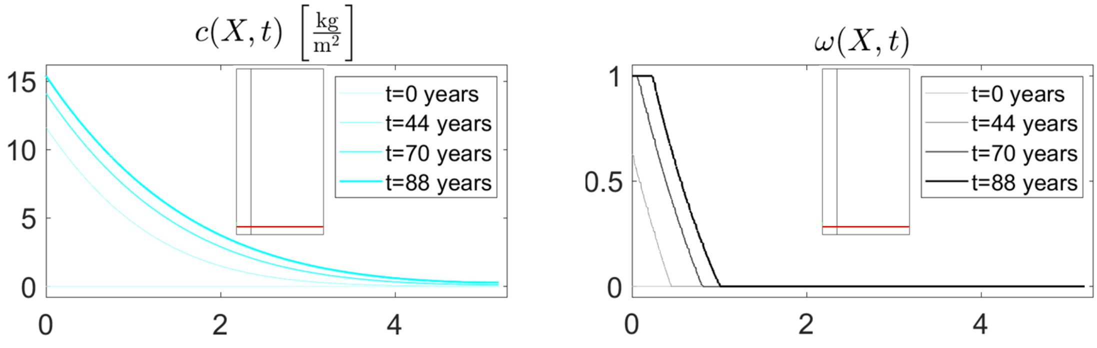

Figure 6. Concentration (left) and damage (right) along the section line (red line) with $X_2 = 0.5\mathrm{m}$ for different times.

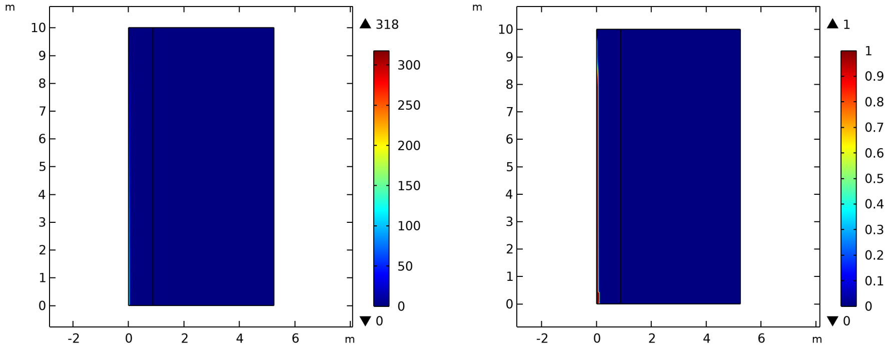

Figure 7. Colour plot of concentration c [kg/m^2] (left) and damage ω (right) for $K^{\mathrm{DIF}} = 10^8 \mathrm{m}^6/\mathrm{kg}\cdot\mathrm{s}$ at the final time $t \approx 27$ years.

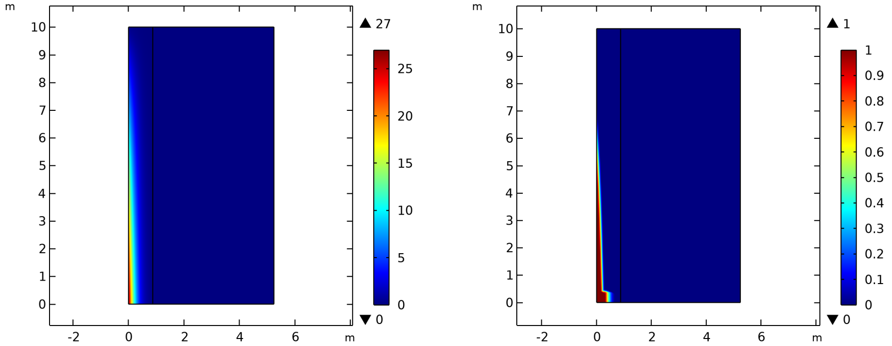

Figure 8. Colour plot of concentration c [kg/m^2] (left) and damage ω (right) for $K^{\mathrm{DIF}} = 10^{10}\, \mathrm{m}^6/\mathrm{kg}\cdot\mathrm{s}$ at the final time $t \approx 19$ years.

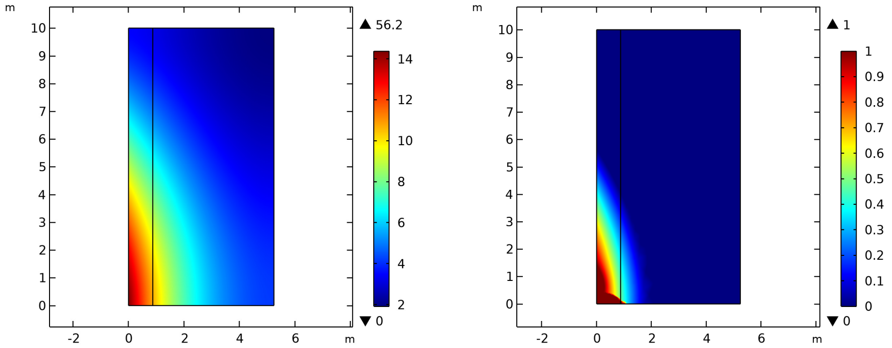

Figure 9. Colour plot of concentration c [kg/m^2] (left) and damage ω (right) for $K^{\mathrm{DIF}} = 2 \cdot 10^{11}\, \mathrm{m}^6/\mathrm{kg}\cdot\mathrm{s}$ at the final time $t \approx 228$ years.

3.1.1. *Parametric analysis:* K^{DIF}. As shown in Figures 7, 8, and 9, the diffusion coefficient K^{DIF} provides a measure of the permeability of water within the body. The figures are colour plots of concentration c on the left side and damage ω on the right side, for different values of K^{DIF}. A parametric analysis was conducted by examining both smaller (Figures 7 and 8) and larger (Figure 9) values of K^{DIF} compared to

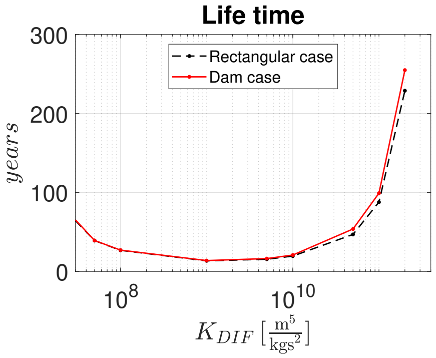

Figure 10. Lifetime of $\mathcal{B}$ as K^{DIF} varies.

the reference value reported in Table 1 (Section 3.1) to investigate its influence. Figures 7 and 8 show that for smaller values of the diffusion coefficient, the lifetime of the body is inversely proportional to K^{DIF}. This behaviour is expected since the fluid cannot easily spread into the material, limiting the increase in the percentage of the damaged area: the concentration of the damaging fluid c reaches very high values but remains confined to a limited region of the body $\mathcal{B}$. Consequently, as the diffusion coefficient K^{DIF} increases, the fluid can spread in a larger region of the body $\mathcal{B}$ and it requires less time to increase the percentage of the damaged area. This trend is evident in Figures 7 and 8 and on the left side of the dashed line in Figure 10, which shows the dependence of the lifetime on K^{DIF}. Thus, as the fluid spreads more easily throughout a larger portion of the body $\mathcal{B}$, the damage ω also reaches its maximum value of 1 over a larger area of $\mathcal{B}$.

The decreasing trend in lifetime is no longer observed for higher values of K^{DIF}. After reaching a minimum value (as shown in the remaining portion of the dashed line in Figure 10), the trend reverses, and lifetime becomes an increasing function of K^{DIF}. This phenomenon can be explained by the fact that higher permeability leads to a more widespread distribution of the fluid (see Figure 9, left), thereby reducing the growth rate within the domain. In turn, this lower diffusion rate of the fluid corresponds to a slower damage growth rate, reducing the temporal evolution of the damage ω.

An increase in the diffusion coefficient K^{DIF} influences fluid diffusion within the body and, consequently, affects damage evolution. Figures 7, 8, and 9 show that for higher values of K^{DIF}, the damage ω concentrates at the base and spreads horizontally. This contrasts with the behaviour observed for smaller values of K^{DIF}, where fluid propagation within the body $\mathcal{B}$ is hindered, causing it to accumulate near the interface boundary in contact with the fluid (left side).

3.1.2. *Parametric analysis: $K_{c\omega}$.* One more parametric analysis is conducted with respect to the concentration-damage coupling factor $K_{c\omega}$. This term links the fluid concentration within the body $\mathcal{B}$ to the damage of the body itself. The greater the magnitude of the negative coupling factor — note that $K_{c\omega} < 0$ as in (40) — the sooner damage evolution begins under the same external loads. The analysis was carried out by systematically varying the value of parameter $K_{c\omega}$, while keeping all other parameters fixed at the values given in Table 1. Concentration c and damage ω for further two different values of $K_{c\omega}$ are shown:

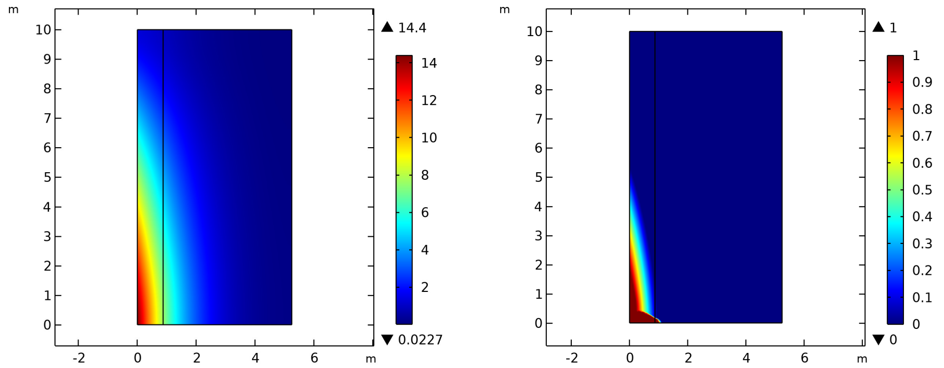

Figure 11. Colour plot of concentration c [kg/m^2] (left) and damage ω (right) for $K_{c\omega} = -5.5\,\mathrm{m}^2/\mathrm{s}^2$ at the final time $t \approx 70$ years.

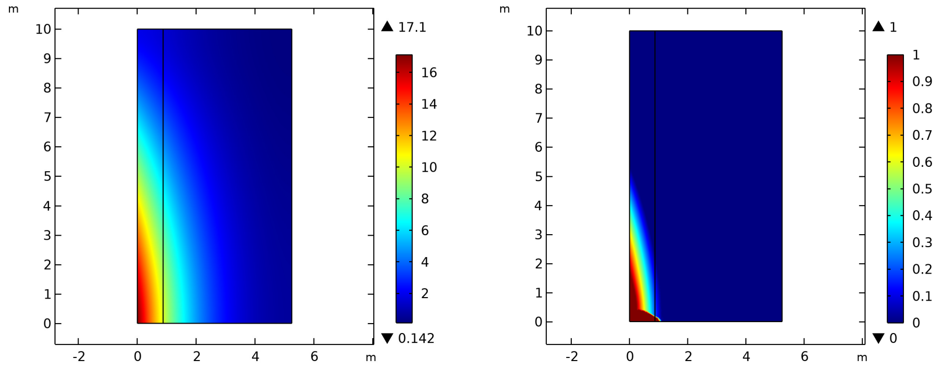

Figure 12. Colour plot of concentration c [kg/m^2] (left) and damage ω (right) for $K_{c\omega} = -4.5\,\mathrm{m}^2/\mathrm{s}^2$ at the final time $t \approx 113$ years.

$K_{c\omega} = -5.5\,\mathrm{m}^2/\mathrm{s}^2$ in Figure 11 and for $K_{c\omega} = -4.5\,\mathrm{m}^2/\mathrm{s}^2$ in Figure 12.

The damage parameter ω is strongly influenced by the concentration-damage coupling factor $K_{c\omega}$. As clearly shown in Figures 11 and 12, even small variations in $K_{c\omega}$ lead to significant changes in the lifetime. This parameter warrants further investigation for future developments, as it can be influenced by the chemical composition of both the body $\mathcal{B}$ and the damaging fluid, and their interaction.

3.2. ***Trapezoidal dam case.*** In this section a realistic trapezoidal gravity dam case is shown. Also for this case we choose to split the domain to optimize the sizes of the mesh. Figure 13 shows the mesh. The area in which the mesh must be finer is that one near the upstream boundary, on the left.

The investigated shape has the follow characteristics: the upstream face is vertical instead the downstream face has usually a uniform slope transitioning to a vertical face near the crest. The slope is usually in the range from 0.7 to 0.8. In the next example the crest is assumed to have a width of 3 m (for allowing the transit of vehicles) and a height of 2 m. Aside from the aforementioned geometric differences, the other parameters listed in Table 1, are unchanged. The shape presented here exhibits greater resistance to external loads due to a more efficient distribution of the bearing capacity. The reason is that a larger

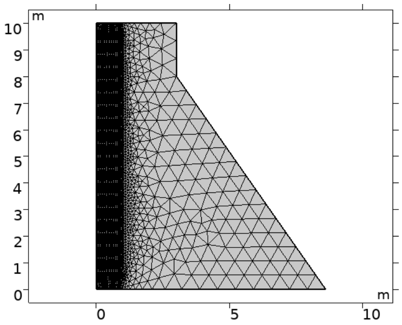

Figure 13. Mesh representation of the trapezoidal domain, which is discretised into elements with side lengths of up to 67 cm, while the subdomain on the left is further refined with elements having maximum side lengths of 5 cm.

area is under compressive stress conditions, and therefore it responds with an higher damage threshold as defined in (9). As a consequence a significantly reduction in the displacements is shown both at the initial elastic stage (see left panes of Figures 3–4 and 14–15) and at the final damaged stage (right panes).

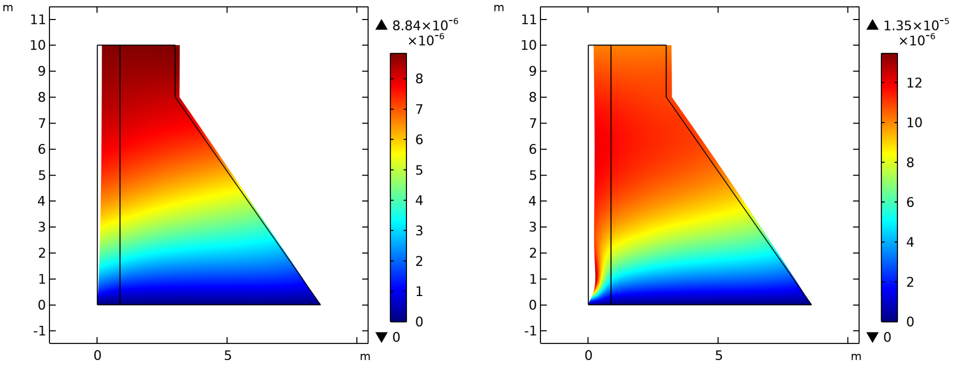

Figure 14. Colour plot of horizontal displacement u_1 [m] in the deformed configuration: initial time (left) and final time $t \approx 99$ years (right).

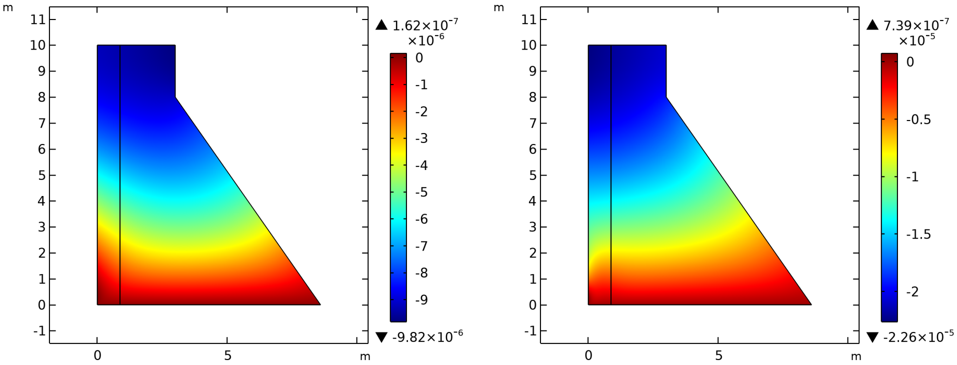

Figure 15. Colour plot of vertical displacement u_2 [m]: initial time (left) and final time $t \approx 99$ years (right).

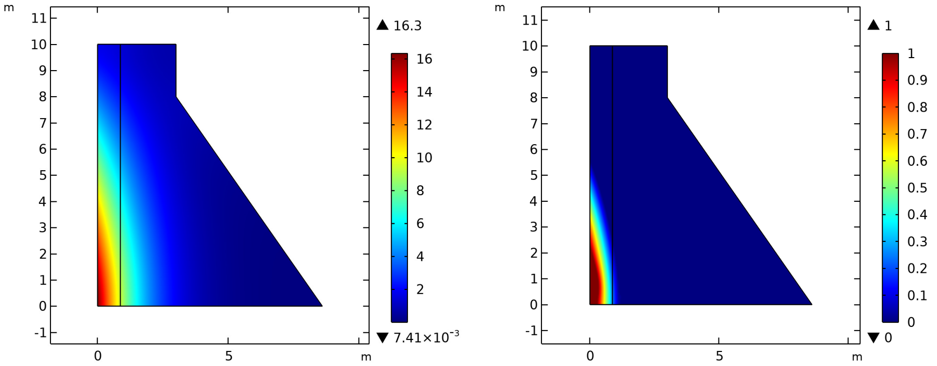

Figure 16. Colour plot of concentration c [kg/m^2] (left) and damage ω (right) at the final time $t \approx 99$ years.

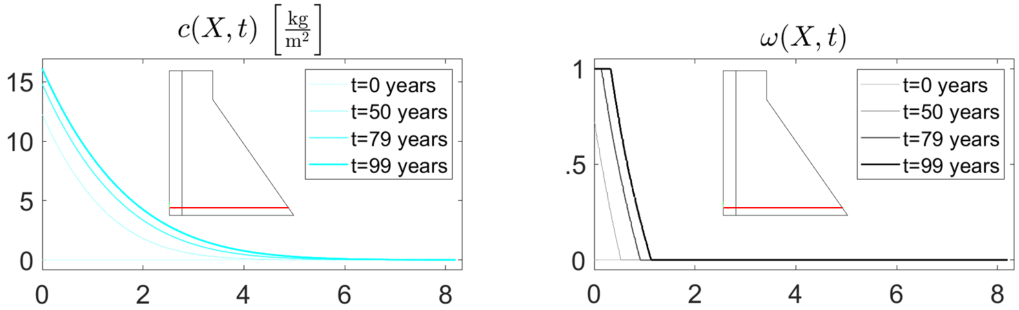

Figure 17. Concentration c and damage ω along the section line (red line) with $X_2 = 0.5$ m for different times.

As for the rectangular case, concentration c and damage ω evolve in a similar way but, in this case, the damage needs a longer time to propagate through the section because, as previously noted, the compressive stress state is associated with a higher damage yielding point $K_{\omega 0}$, enabling the body to better resist the onset of damage. This is why its lifetime is significantly longer than in the rectangular case.

The evolution of concentration c and damage ω for a section with coordinates $X_2 = 0.5$m are shown in Figure 17.

3.2.1. *Parametric analysis:* K^{DIF}. As in Section 3.1.1, concentration c and damage ω distributions are presented for different values of the diffusion coefficient K^{DIF} in the trapezoidal domain. The results are shown in Figures 18, 19 and 20. As for the rectangular case, also for the trapezoidal one the considered values of the diffusion coefficient, in order to carry out the parametric analysis, are chosen both smaller (Figures18–19) and higher (Figure 20).

The behaviour remains analogous to the rectangular case when varying the diffusion coefficient K^{DIF}. Indeed, from the figures 18, 19 and 20 one notes that, when the diffusion coefficient K^{DIF} increases, the lifetime of the structure does not always increase. The motivation is the same we explained for the rectangular case in Section 3.1.1: when the diffusion coefficient is relatively high, the fluid can spread

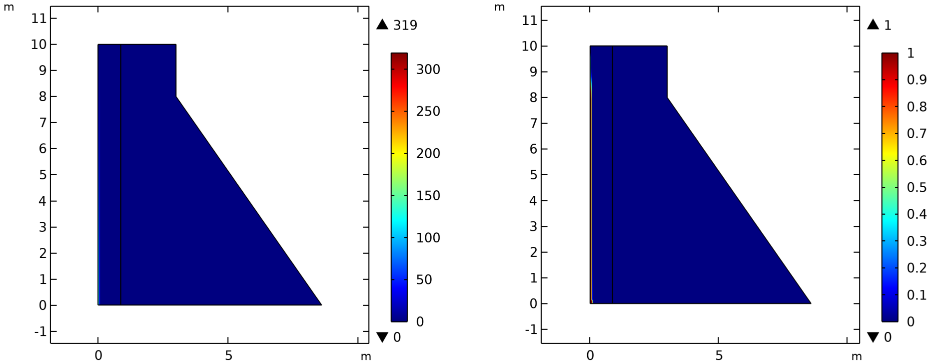

Figure 18. Colour plot of concentration c [kg/m^2] (left) and damage ω for $K^{\mathrm{DIF}} = 10^8$ m^6/kg $\cdot$ s at the final time $t \approx 27$ years.

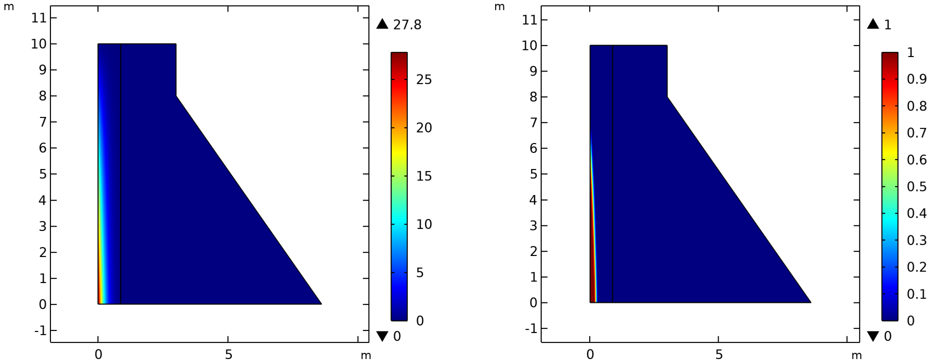

Figure 19. Colour plot of concentration c [kg/m^2] (left) and damage ω for $K^{\mathrm{DIF}} = 10^{10}$ m^6/kg $\cdot$ s at the final time $t \approx 21$ years.

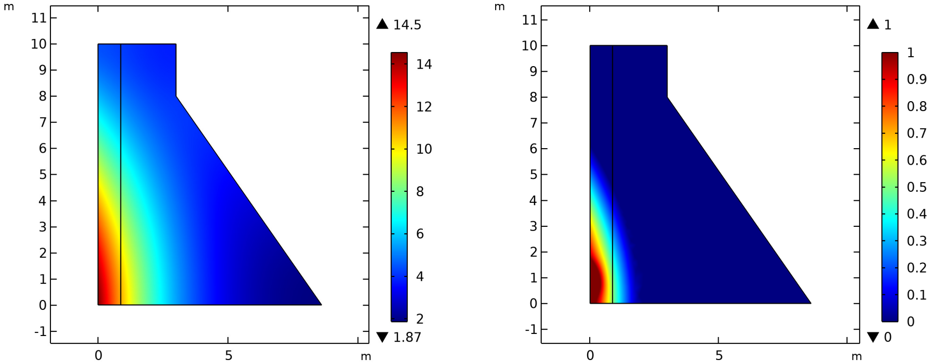

Figure 20. Colour plot of concentration c [kg/m^2] (left) and damage ω for $K^{\mathrm{DIF}} = 2 \cdot 10^{11}$ m^6/kg $\cdot$ s ath the final time $t \approx 255$ years.

across a larger area of body $\mathcal{B}$, by inducing a slower evolution rate of the damaging fluid concentration c. This slows down the damage diffusion process. Instead, when diffusion coefficient is relatively smaller, the impermeability restricts the ability of the fluid to permeate the structure. Consequently, the damaged

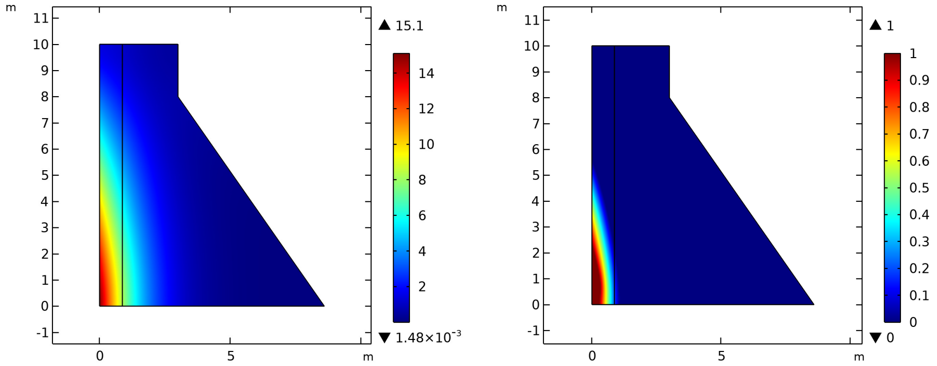

Figure 21. Colour plot of concentration $c[\mathrm{kg/m^2}]$ (left) and damage ω for $K_{c\omega} = 5.5\,\mathrm{m^2/s^2}$ at the final time $t \approx 80$ years.

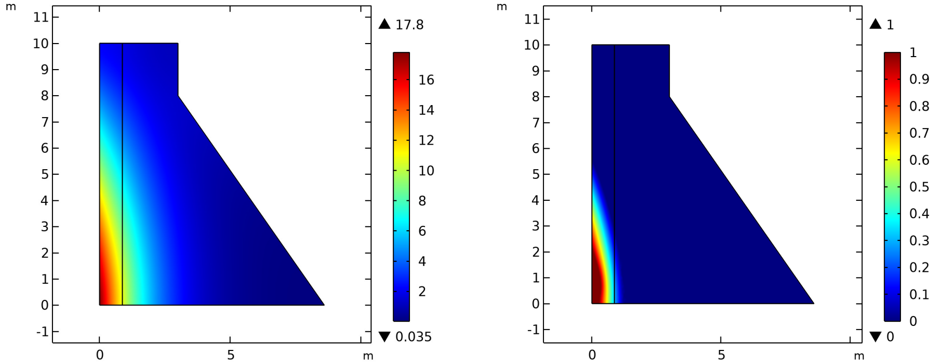

Figure 22. Colour plot of concentration $c[\mathrm{kg/m^2}]$ (left) and damage ω for $K_{c\omega} = 4.5\,\mathrm{m^2/s^2}$ at the final time $t \approx 128$ years.

area reaches a limit that cannot be exceeded if K^{DIF} is sufficiently small. So, as it is shown in the continuous line in Figure 10, the lifetime of the body $\mathcal{B}$ exhibits a minimum with respect to the diffusion coefficient K^{DIF}. As observed in the rectangular case (Section 3.1.1), the damaged zone propagates from the structure-fluid interface towards the base.

3.2.2. *Parametric analysis:* $K_{c\omega}$. As for the rectangular case shown in Section 3.1.2, the parametric analysis in terms of the concentration-damage coupling factor $K_{c\omega}$ is here presented. In the following the concentration c and the damage ω for different values of $K_{c\omega}$ (one higher and one smaller than the main example shown in Section 3.2) are presented. Also for this case the aforementioned analysis aims to elucidate the role of $K_{c\omega}$ and quantify the extent to which this parameter influences the evolution of damage. The different values of $K_{c\omega}$ are, like for the rectangular case, $K_{c\omega} = -5.5\,\mathrm{m^2/s^2}$ in Figure 21 and $K_{c\omega} = -4.5\,\mathrm{m^2/s^2}$ in Figure 22.

3.3. ***Comparison.*** Some comparisons are reported here between the two cases analysed above (rectangular and trapezoidal cases) which show how the stockier shape continues to have a better mechanical response. The comparison are carried out in terms of lifetime of the dam. In Figure 23 the evolution of the damaged

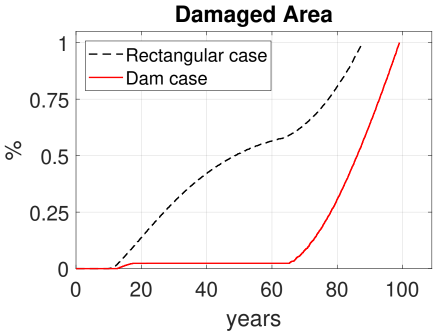

Figure 23. Evolution of the damaged area in time for the rectangular and the trapezoidal cases.

area in time of the body $\mathcal{B}$ is shown for both the rectangular (dashed black line) and the trapezoidal cases (continuous red line). As can be easily observed, the rectangular case takes less time to reach 1% of damaged area (and the difference between the two cases is around 15%). Besides, the evolution of damage for the rectangular case starts at the very beginning of the lifetime and that for the trapezoidal case after more than 50 years.

The evolution of the lifetime of the dam, shown in Section 3.1 (Figures 7, 8 and 9) and in Section 3.2 (Figures 18, 19 and 20) is summarised in Figure 10. As expected, the lifetime of body $\mathcal{B}$ exhibits a decreasing trend for lower diffusivity values of K^{DIF} and, after reaching a minimum, it starts again to increase. This behaviour is highly realistic because for lower diffusivity values of K^{DIF}, the fluid remains confined to the left boundary of the interface and, being unable to diffuse easily, the concentration c reaches remarkably high values in a relatively confined area. Consequently, through the concentration-damage coupling factor $K_{c\omega}$, the damage ω also spreads slowly, leading to a very slow attainment of the imposed limit (1% of the total area). Conversely, when the diffusion coefficient increases beyond a certain range, the fluid penetrates and spreads more easily into the body, causing the same amount of fluid to distribute over a larger region, thus reducing the concentration rate in the affected area. This smaller value of the growth rate of c clearly corresponds to a slower growth rate of the damage ω. Bigger differences (around 15%) are observable for the extreme values of K^{DIF} (see Figures 10 and 24).

Denoting, for each value of the diffusion coefficient K^{DIF}, the lifetime of the realistic trapezoidal dam case as t_d and the lifetime of the rectangular case as t_r, the percentage difference is calculated as follows:

$$D = 100\frac{t_d - t_r}{t_r}. \tag{44}$$

It can be seen in Figure 24 that the difference D in lifetime is negligible within the range of K^{DIF} between $5 \cdot 10^8\ \mathrm{m}^6/\mathrm{kg}\cdot\mathrm{s}$ and $10^9\ \mathrm{m}^6/\mathrm{kg}\cdot\mathrm{s}$. However, as already depicted in Sections 3.1.1 and 3.2.1, it becomes more pronounced for the higher values of K^{DIF}.

In Figures 25 and 26 the plot of the evolution of both the eigenvalues and the trace of the strain tensor $\mathbb{G}$ is shown respectively for the rectangular and trapezoidal cases. Both the colour map and the legend are scaled to be always negative, thus enhancing the visibility of the compressive regions. Comparing the

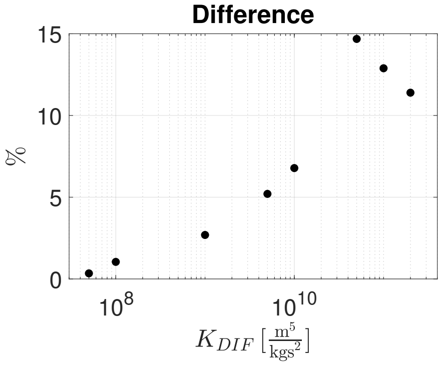

Figure 24. Percentage difference in lifetime of the body $\mathcal{B}$ between the two different shapes (rectangular and trapezoidal ones) as K^{DIF} varies.

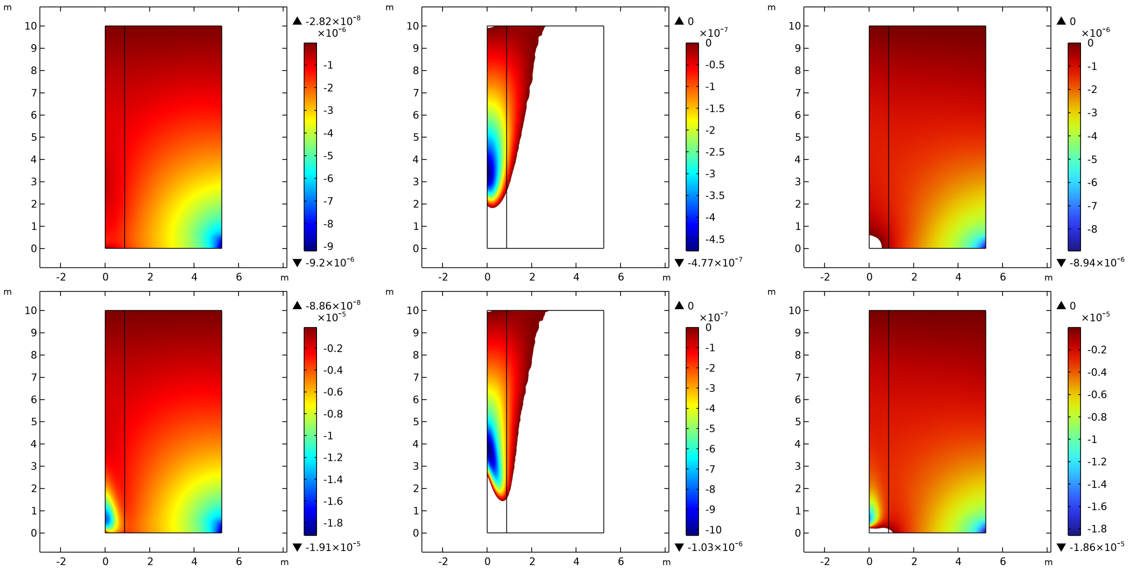

Figure 25. Properties of $\mathbb{G}$ at initial (upper row) and final (lower row) times: least eigenvalue (left), highest eigenvalue (middle column) and trace (right).

right columns of Figures 25 and 26, we see a substantial difference in terms of the extent of the area subjected to tension. In the rectangular case, a significant portion of the domain, particularly at the base, is found to be in tension ($\mathrm{tr}\,\mathbb{G} > 0$). The trapezoidal case exhibits a significantly different response; the figures reveal that the trapezoidal shape ensures that the entire structure is always under compression, thus justifying the shape largely used in the design of gravity dams.

4. Conclusion

Different approaches have been used in literature in order to study the diffusion of ions into a body as in [35; 34]. The proposed formulation utilises an energy functional specified in (11) and the hemivariational principle to simulate the coupled phenomenon of an damaging fluid diffusion and damage-induced

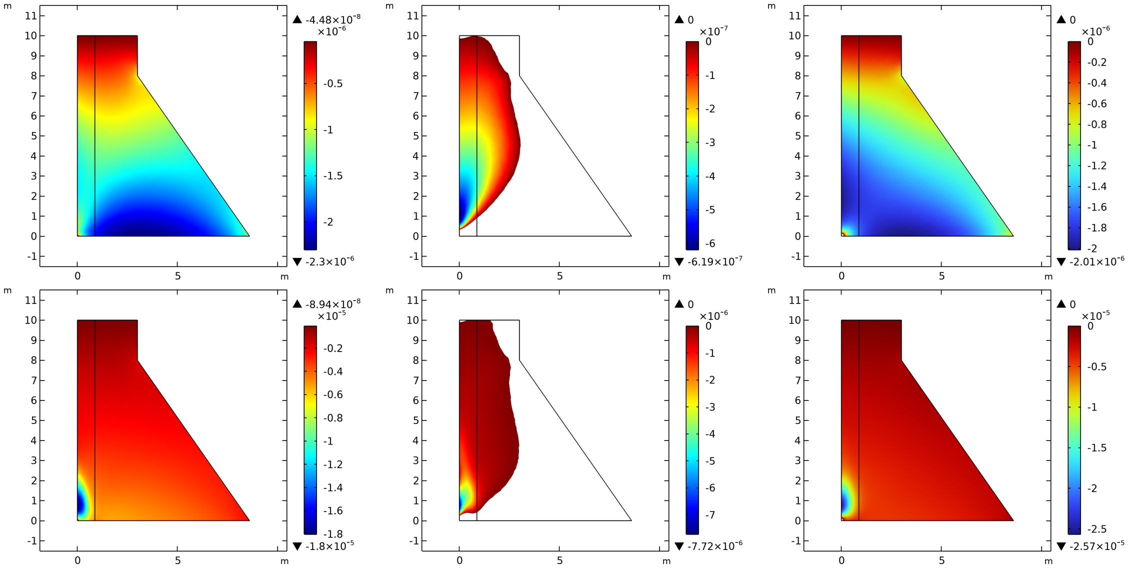

Figure 26. Properties of $\mathbb{G}$ at initial (upper row) and final (lower row) times: least eigenvalue (left), highest eigenvalue (middle column) and trace (right).

mechanical deterioration. Specifically, using the considered hemivariational principle, it was possible to include damage as a monotonically increasing function, that goes from 0 (non damaged case) to 1 (complete failure), which causes the stiffnesses to fall as shown in the Section 3. The contribution of second-gradient terms [49] was also considered, enriching the formulation of the energy functional and the Karush–Kuhn–Tucker conditions, thus providing a more refined model. By means of the concentration-damage coupling factor $K_{c\omega}$, which appear in the last row of the (11), the damage and the diffusion of the fluid (within the body $\mathcal{B}$) are coupled; in this way the spreading of the fluid into the structure causes increasing of the damage and it contributes to failure. In Sections 3.1.1, 3.1.2, 3.2.1 and 3.2.2 the role of the diffusion coefficient K^{DIF} and of the concentration-damage coupling factor $K_{c\omega}$ are shown. The diffusion coefficient, in particular, represents a parameter that influences the spreading of the fluid within the body. As shown in this paper, the damage is affected not only by the changes of K^{DIF} but also by small changes of $K_{c\omega}$. Increasing $K_{c\omega}$ (decrease in the value of its modulus), the failure of the structure is delayed. The work presented here is the next step of the already published [70] one-dimensional case and the hemivariational method used in [62]. A future goal will be to take into account this diffusion theory for the granular micromechanics approach [74] so as to properly analyse the material of which the dams are composed, such as concrete [63]. A further improvement could be to correlate the diffusion coefficient, K^{DIF}, with damage, ω. This is motivated by the observation that in brittle materials such as concrete [26; 27], where failure occurs and cracks propagate [13; 3; 1], fluid diffusion is facilitated due to increased porosity [40]. More specifically, the present work is part of a research project regarding the modelling of elastic, plastic and damaging phenomena in granular materials through hemivariational inequalities. This project started from thermomechanical analyses of granular interactions [56], before being reformulated through a hemivariational principle accounting for elastic, plastic and damaging phenomena [62; 61; 74]. This approach has been applied to many types of systems which can be modelled as having granular interactions at a local scale, such as reinforced concrete [64; 66; 41; 43] or masonry structures [75; 42], among others. It is worth noting that the study of the diffusion of an aging agent within an human made construct is not limited to the case of dams but can find many applications in each field of the civil engineering (for example the major infrastructures and geotechnical works). Furthermore, it should be noted that this formulation has a wide range of applications extending beyond the field of civil engineering [72; 67; 2; 12], as the phenomenon of diffusion is a cross-cutting topic that encompasses various fields such as medicine [57; 54] and geology. It could help, for example, in the monitoring and safeguarding of the objects of artistic-cultural heritage [36] and to allow for more careful design of future structures aimed at protecting the artifacts from the diffusion of slag [44; 73] or pollutants that abound in our cities.

The work presented here aims to contribute to the estimation of the service life of a dam body and, more generally, to the assessment of damage in structures interacting with a fluid. The variational nature of the proposed model, together with the absence of restrictive initial assumptions, allows for its application to a broad range of problems. In the current formulation, the parameters have been selected to ensure isotropic behaviour, regardless of the damage state. However, it is reasonable to expect that damage may induce anisotropic effects. A natural development of this work will thus involve the introduction of anisotropy into the model, with the goal of enhancing its realism. Anisotropy could be characterised, for example: by extending the diffusion coefficient from a scalar to a tensor, allowing for direction-dependent diffusion behaviour; by introducing mechanically induced anisotropy due to damage, which could be modelled using a granular mechanics framework. Furthermore, the diffusion coefficient and the coupling factor between concentration and damage should be investigated in more detail to obtain more realistic estimates. These parameters could be identified through experimental measurements on real structures or laboratory-scale models. Another relevant development would be to introduce a direct coupling between the diffusion coefficient and the damage state, as it is plausible that damaged regions allow for increased fluid flow not primarily due to capillarity, but rather due to increased porosity and, consequently, permeability. The dissipation functional employed, which yields a standard diffusion equation, was chosen for its simplicity rather than its specificity to the problem at hand. In particular, the Rayleigh-type dissipation functional used in this study results in a diffusion coefficient that is independent of the damage state. Future work will focus on applying the model to specific case studies, allowing for a more refined characterisation of both elastic energy and dissipation functionals (rate-independent and rate-dependent) both in terms of coefficient values and in the functional forms themselves.

Acknowledgement

The research reported in the present contribution was carried out as part of the project A Fluid-Structure Interaction tool for the protection of Clean Energy Production sites (FSI-CEP) funded by the MUR Progetti di Ricerca di Rilevante Interesse Nazionale (PRIN) Bando 2022 PNRR - grant P20227CSJ5.

References

[1] B. E. Abali, "Phase-field damage modeling in generalized mechanics by using a mixed finite Element method (FEM)", pp. 1–18 in *Creep in structures VI*, edited by H. Altenbach and K. Naumenko, Springer, 2023.

[2] B. E. Abali, J. Vorel, and R. Wan-Wendner, "Thermo-mechano-chemical modeling and computation of thermosetting polymers used in post-installed fastening systems in concrete structures", *Contin. Mech. Therm.* **35**:3 (2023), 971–989.

[3] B. Amirian, B. E. Abali, and J. D. Hogan, "The study of diffuse interface propagation of dynamic failure in advanced ceramics using the phase-field approach", *Comput. Methods Appl. Mech. Eng.* **405** (2023), art. id. 115862, 18 pp.

[4] D. Ammendolea, F. Greco, P. Lonetti, R. Luciano, and A. Pascuzzo, "Crack propagation modeling in functionally graded materials using Moving Mesh technique and interaction integral approach", *Compos. Struct.* **269** (2021), art. id. 114005.

[5] C. Ancey, S. Cochard, and N. Andreini, "The dam-break problem for viscous fluids in the high-capillary-number limit", *J. Fluid Mech.* **624** (2009), 1–22.

[6] G. Aretusi, C. Cardillo, A. Salvatori, E. Bednarczyk, and R. Fedele, "A simple extension of Timoshenko beam model to describe dissipation in cementitious elements", *Z. Angew. Math. Phys.* **75**:5 (2024), art. id. 166, 22 pp.

[7] N. Auffray, F. dell'Isola, V. A. Eremeyev, A. Madeo, and G. Rosi, "Analytical continuum mechanics *à la* Hamilton–Piola least action principle for second gradient continua and capillary fluids", *Math. Mech. Solids* **20**:4 (2015), 375–417.

[8] E. Barchiesi and N. Hamila, "Maximum mechano-damage power release-based phase-field modeling of mass diffusion in damaging deformable solids", *Z. Angew. Math. Phys.* **73**:1 (2022), art. id. 35, 21 pp.

[9] E. Barchiesi, A. Misra, L. Placidi, and E. Turco, "Granular micromechanics-based identification of isotropic strain gradient parameters for elastic geometrically nonlinear deformations", *Z. Angew. Math. Mech.* **101**:11 (2021), art. id. e202100059, 21 pp.

[10] J. A. Bather, "A diffusion model for the control of a dam", *J. Appl. Probability* **5** (1968), 55–71.

[11] E. Bosco, A. S. J. Suiker, and N. A. Fleck, "Crack channelling mechanisms in brittle coating systems under moisture or temperature gradients", *Int. J. Fract.* **225** (2020), 1–30.

[12] A. Bossio, F. Fabbrocino, T. Monetta, G. P. Lignola, A. Prota, G. Manfredi, and F. Bellucci, "Corrosion effects on seismic capacity of reinforced concrete structures", *Corrosion Rev.* **37**:1 (2019), 45–56.

[13] D. Castillo, T. H. Nguyen, and J. Niiranen, "Spatially random modulus and tensile strength: contribution to variability of strain, damage, and fracture in concrete", *Int. J. Damage Mech.* **30**:10 (2021), 1497–1523.

[14] N. Cefis and C. Comi, "Damage modelling in concrete subject to sulfate attack", *Frattura Integr. Strutt.* **8**:29 (2014), 222–229.

[15] N. Cefis and C. Comi, "Chemo-mechanical modelling of the external sulfate attack in concrete", *Cem. Concr. Res.* **93**:2017 (2017), 57–70.

[16] O. Chekeres, V. Salnikov, and F. D'Annibale, "From approximation of dissipative systems to representative space-time volume elements for metamaterials", *Contin. Mech. Therm.* **36**:6 (2024), 1597–1605.

[17] D. Chen, B. Huang, and F. Kang, "A review of detection technologies for underwater cracks on concrete dam surfaces", *App. Sci.* **13**:6 (2023), art. id. 3564.

[18] A. Ciallella, D. Pasquali, M. Gołaszewski, F. D'Annibale, and I. Giorgio, "A rate-independent internal friction to describe the hysteretic behavior of pantographic structures under cyclic loads", *Mech. Res. Commun.* **116** (2021), art. id. 103761.

[19] A. Ciallella, D. Pasquali, F. D'Annibale, and I. Giorgio, "Shear rupture mechanism and dissipation phenomena in bias-extension test of pantographic sheets: numerical modeling and experiments", *Math. Mech. Solids* **27**:10 (2022), 2170–2188.

[20] A. Ciallella, D. Scerrato, M. Spagnuolo, and I. Giorgio, "A continuum model based on Rayleigh dissipation functions to describe a Coulomb-type constitutive law for internal friction in woven fabrics", *Z. Angew. Math. Phys.* **73**:5 (2022), art. id. 209, 17.

[21] M. Colombo and C. Comi, "Hydro-thermo-mechanical analysis of an existing gravity dam undergoing alkali-silica reaction", *Infrastructures* **4**:3 (2019).

[22] C. Comi, R. Fedele, U. Perego, et al., "Modelling concrete degradation in dams due to alkali-aggregate reaction", in *Proceedings of the* 9th *US National Conference on Computational Mechanics*, 2007.

[23] C. Comi, R. Fedele, and U. Perego, "A chemo-thermo-damage model for the analysis of concrete dams affected by alkali-silica reaction", *Mech. Mater.* **41**:3 (2009), 210–230.

[24] M. Cuomo, "Continuum damage model for strain gradient materials with applications to 1D examples", *Contin. Mech. Therm.* **31**:4 (2019), 969–987.

[25] H. Darban, R. Luciano, A. Caporale, and F. Fabbrocino, "Higher modes of buckling in shear deformable nanobeams", *Int. J. Eng. Sci.* **154** (2020), art. id. 103338, 18 pp.

[26] U. De Maio, D. Gaetano, F. Greco, R. Luciano, and A. Pranno, "Degradation analysis of dynamic properties for plain concrete structures under mixed-mode fracture conditions via an improved cohesive crack approach", *Fracture Struct. Integ.* **18**:68 (2024), 422–439.

[27] U. De Maio, F. Greco, L. Leonetti, R. Luciano, P. Nevone Blasi, and S. Vantadori, "A refined diffuse cohesive approach for the failure analysis in quasibrittle materials, II: Application to plain and reinforced concrete structures", *Fatigue Fracture Eng. Mater. Struct.* **42**:12 (2019), 2764–2781.

[28] F. dell'Isola, I. Giorgio, M. Pawlikowski, and N. L. Rizzi, "Large deformations of planar extensible beams and pantographic lattices: heuristic homogenization, experimental and numerical examples of equilibrium", *Proc. R. Soc. Lond. A* **472**:2185 (2016).

[29] F. dell'Isola and L. Placidi, "Variational principles are a powerful tool also for formulating field theories", pp. 1–15 in *Variational models and methods in solid and fluid mechanics*, CISM Courses and Lect **535**, Springer, 2011.

[30] F. dell'Isola, P. Seppecher, L. Placidi, E. Barchiesi, and A. Misra, "Least action and virtual work principles for the formulation of generalized continuum models", pp. 327–394 in *Discrete and continuum models for complex metamaterials*, Cambridge University Press, 2020.

[31] F. dell'Isola, P. Seppecher, M. Spagnuolo, E. Barchiesi, F. Hild, T. Lekszycki, I. Giorgio, L. Placidi, U. Andreaus, M. Cuomo, et al., "Advances in pantographic structures: design, manufacturing, models, experiments and image analyses", *Contin. Mech. Therm.* **31**:4 (2019), 1231–1282.

[32] F. dell'Isola and C. Woźniak, "On phase transition layers in certain micro-damaged two-phase solids", *Int. J. Fract.* **83**:2 (1997), 175–189.

[33] V. A. Eremeyev, F. dell'Isola, C. Boutin, and D. Steigmann, "Linear pantographic sheets: existence and uniqueness of weak solutions", *J. Elasticity* **132**:2 (2018), 175–196.

[34] G. J. A. M. Eumelen, E. Bosco, A. S. J. Suiker, and J. J. Hermans, "Chemo-mechanical model for degradation of oil paintings by amorphous and crystalline metal soaps", *Eur. J. Mech. A Solids* **97** (2023), art. id. 104827, 17 pp.

[35] G. J. A. M. Eumelen, E. Bosco, A. S. J. Suiker, A. van Loon, and P. D. Iedema, "A computational model for chemo-mechanical degradation of historical oil paintings due to metal soap formation", *J. Mech. Phys. Solids* **132** (2019), art. id. 103683, 21 pp.

[36] G. J. A. M. Eumelen, E. Bosco, S. J. Suiker, Akke, J. J. Hermans, A. van Loon, K. Keune, and P. D. Iedema, "Computational modelling of metal soap formation in historical oil paintings: the influence of fatty acid concentration and nucleus geometry on the induced chemo-mechanical damage", *SN Appl. Sci.* **2**:7 (2020).

[37] M. F. Funari, S. Spadea, F. Fabbrocino, and R. Luciano, "A moving interface finite element formulation to predict dynamic edge debonding in FRP-strengthened concrete beams in service conditions", *Fibers* **8**:6 (2020).

[38] L. Gallucci, C. Menna, L. Angrisani, D. Asprone, R. Schiano Lo Moriello, F. Bonavolontà, and F. Fabbrocino, "An embedded wireless sensor network with wireless power transmission capability for the structural health monitoring of reinforced concrete structures", *Sensors* **17**:11 (2017), art. id. 2566.

[39] I. Giorgio, "A variational formulation for one-dimensional linear thermoviscoelasticity", *Math. Mech. Complex Syst.* **9**:4 (2021), 397–412.

[40] I. Giorgio, F. dell'Isola, U. Andreaus, F. Alzahrani, T. Hayat, and T. Lekszycki, "On mechanically driven biological stimulus for bone remodeling as a diffusive phenomenon", *Biomech. Model. Mechanobiol.* **18**:6 (2019).

[41] F. Greco, L. Leonetti, and R. Luciano, "A multiscale model for the numerical simulation of the anchor bolt pull-out test in lightweight aggregate concrete", *Constr. Build. Mater.* **95** (2015), 860–874.

[42] F. Greco, L. Leonetti, R. Luciano, A. Pascuzzo, and C. Ronchei, "A detailed micro-model for brick masonry structures based on a diffuse cohesive-frictional interface fracture approach", *Procedia Structural Integrity* **25** (2020), 334–347.

[43] A. Grimaldi and R. Luciano, “Tensile stiffness and strength of fiber-reinforced concrete”, *J. Mech. Phys. Solids* **48**:9 (2000), 1987–2008.

[44] C. Guo, B. Sun, D. Hu, F. Wang, M. Shi, and X. Li, “A Field Experimental Study on the Diffusion Behavior of Expanding Polymer Grouting Material in Soil”, *Soil Mech. Foundation Engng.* **56** (2019).

[45] C. C. Habeger, D. W. Coffin, and B. Hojjatie, “Influence of humidity cycling parameters on the moisture-accelerated creep of polymeric fibers”, *J. Polym. Sci. B Polym. Phys.* **39**:17 (2001), 2048–2062.

[46] M. A. Hariri-Ardebili and V. E. Saouma, “Collapse fragility curves for concrete dams: comprehensive study”, *J. Struct. Eng.* (*ASCE*) **142**:10 (2016), art. id. 04016075.

[47] T. Hromadka, C. Berenbrock, J. Freckleton, and G. Guymon, “A two-dimensional dam-break flood plain model”, *Adv. Water Resources* **8**:1 (1985), 7–14.

[48] F. Javanmardi and P. Léger, “Grouting of cracks in concrete dams: numerical modelling and structural behaviour”, *Prog. Struct. Eng. Mater.* **7**:4 (2005), 161–173.

[49] S. Khakalo and J. Niiranen, “Form II of Mindlin’s second strain gradient theory of elasticity with a simplification: for materials and structures from nano- to macro-scales”, *Eur. J. Mech. A Solids* **71** (2018), 292–319.

[50] F. Kiakojouri, V. De Biagi, M. Marchelli, and B. Chiaia, “A conceptual note on the definition of initial failure in progressive collapse scenarios”, *Structures* **60** (2024), art. id. 105921.

[51] F. Kiakojouri, M. R. Sheidaii, V. De Biagi, and B. Chiaia, “Progressive collapse of structures: a discussion on annotated nomenclature”, *Structures* **29** (2021), 1417–1423.

[52] D. Liu, M.-j. Lian, C.-w. Lu, and W. Zhang, “Effect of the lenticles on moisture migration in capillary zone of tailings dam”, *Int. J. Min. Metall. Mater.* **27** (2020), 1036–1045.

[53] X. Liu, Z. Li, L. Sun, E. Y. Khailah, J. Wang, and W. Lu, “A critical review of statistical model of dam monitoring data”, *J. Building Eng.* **80** (2023), art. id. 108106.

[54] I. J. Macha, B. Ben-Nissan, E. N. Vilchevskaya, A. S. Morozova, B. E. Abali, W. H. Müller, and W. Rickert, “Drug delivery from polymer-based nanopharmaceuticals: an experimental study complemented by simulations of selected diffusion processes”, *Frontiers Bioeng. Biotech.* **7** (2019), art. id. 37.

[55] R. D. Mindlin, “Micro-structure in linear elasticity”, *Arch. Ration. Mech. Anal.* **16** (1964), 51–78.

[56] A. Misra and P. Poorsolhjouy, “Granular micromechanics model for damage and plasticity of cementitious materials based upon thermomechanics”, *Math. Mech. Solids* **25**:10 (2020), 1778–1803.

[57] A. S. Morozova, E. N. Vilchevskaya, W. H. Müller, and N. M. Bessonov, “Models for drug release of gentamicin in a polylactic acid matrix”, *Math. Mech. Complex Syst.* **8**:4 (2020), 307–320.

[58] E. M. das Neves and A. V. Pinto, “Modelling collapse on rockfill dams”, *Comput. Geotech.* **6**:2 (1988), 131–153.

[59] R. P. L. Nijssen et al., *Fatigue life prediction and strength degradation of wind turbine reactor blade composites*, 2006.

[60] E. Pittella, L. Angrisani, A. Cataldo, E. Piuzzi, and F. Fabbrocino, “Embedded split ring resonator network for health monitoring in concrete structures”, *IEEE Instr. Meas. Mag* **23**:9 (2020), 14–20.

[61] L. Placidi, E. Barchiesi, F. dell’Isola, V. Maksimov, A. Misra, N. Rezaei, A. Scrofani, and D. Timofeev, “On a hemivariational formulation for a 2D elasto-plastic-damage strain gradient solid with granular microstructure”, *Math. Eng* **5**:1 (2023), art. id. 021, 24 pp.

[62] L. Placidi, A. Misra, and E. Barchiesi, “Two-dimensional strain gradient damage modeling: a variational approach”, *Z. Angew. Math. Phys.* **69**:3 (2018), art. id. 56, 19 pp.

[63] A. Pranno, F. Greco, P. Lonetti, R. Luciano, and U. De Maio, “An improved fracture approach to investigate the degradation of vibration characteristics for reinforced concrete beams under progressive damage”, *Int. J. Fatigue* **163** (2022), art. id. 107032.

[64] M. H. G. Rad, M. M. Nayeban, and M. Kazemi, “Externally bonded FRP and mechanically fastened by nailing: a new technique to postpone debonding of FRP sheets in unreinforced concrete slabs”, *Adv. Concrete Construction* **14**:6 (2022), art. id. 413.

[65] K. Rajagopal, A. Srinivasa, and A. Wineman, “On the shear and bending of a degrading polymer beam”, *Int. J. Plast.* **23**:9 (2007), 1618–1636.

[66] N. Rezaei, E. Barchiesi, D. Timofeev, C. A. Tran, A. Misra, and L. Placidi, “Solution of a paradox related to the rigid bar pull-out problem in standard elasticity”, *Mech. Res. Commun.* **126** (2022).

[67] F. A. Rooyackers, E. Bosco, A. S. Suiker, and F. H. Clemens, “A chemo-mechanical model for biogenic sulphide corrosion of concrete”, *Cem. Concr. Res.* **160** (2022), art. id. 106809.

[68] G. Rosi, N. Auffray, and C. Combescure, “On the failure of classic elasticity in predicting elastic wave propagation in gyroid lattices for very long wavelengths”, *Symmetry* **12**:8 (2020).

[69] M. Scaioni, M. Marsella, M. Crosetto, V. Tornatore, and J. Wang, “Geodetic and remote-sensing sensors for dam deformation monitoring”, *Sensors* **18**:11 (2018), art. id. 3682.

[70] A. Scrofani, E. Barchiesi, B. Chiaia, A. Misra, and L. Placidi, “Fluid diffusion related aging effect in a concrete dam modeled as a Timoshenko beam”, *Math. Mech. Complex Syst.* **11**:2 (2023), 313–334.

[71] M. Spagnuolo, K. Barcz, A. Pfaff, F. dell’Isola, and P. Franciosi, “Qualitative pivot damage analysis in aluminum printed pantographic sheets: numerics and experiments”, *Mech. Res. Commun.* **83** (2017), 47–52.

[72] G. Templet and D. Steigmann, “On the theory of diffusion and swelling in finitely deforming elastomers”, *Math. Mech. Complex Syst.* **1**:1 (2013), 105–128.

[73] M. D. Thomas and P. B. Bamforth, “Modelling chloride diffusion in concrete”, *Cem. Concr. Res.* **29**:4 (1999), 487–495.

[74] D. Timofeev, E. Barchiesi, A. Misra, and L. Placidi, “Hemivariational continuum approach for granular solids with damage-induced anisotropy evolution”, *Math. Mech. Solids* **26**:5 (2021), 738–770.

[75] C. A. Tran and E. Barchiesi, “A new block-based approach for the analysis of damage in masonries undergoing large deformations”, *Contin. Mech. Therm.* **35**:4 (2023), 1625–1654.

[76] I. Vlahinić, J. J. Thomas, H. M. Jennings, and J. E. Andrade, “Transient creep effects and the lubricating power of water in materials ranging from paper to concrete and Kevlar”, *J. Mech. Phys. Solids* **60**:7 (2012), 1350–1362.

[77] J. Z. Wang, D. A. Dillard, and F. A. Kamke, “Transient moisture effects in materials”, *J. Mater. Sci.* **26** (1991), 5113–5126.

[78] Y. Yang and A. Misra, “Micromechanics based second gradient continuum theory for shear band modeling in cohesive granular materials following damage elasticity”, *Int. J. Solids Struct.* **49**:18 (2012), 2500–2514.

[79] M. Zucca, E. Reccia, N. Longarini, V. Eremeyev, and P. Crespi, “On the structural behaviour of existing RC bridges subjected to corrosion effects: numerical insight”, *Engng. Failure Anal.* **152** (2023), art. id. 107500.

Received 22 May 2025. Revised 11 Sep 2025. Accepted 22 Oct 2025.

ANGELO SCROFANI: `cangelofani@gmail.com`
Dipartimento di Architettura, Design e Urbanistica, Università degli Studi di Sassari, Alghero, Italy

EMILIO BARCHIESI: `ebarchiesi@uniss.it`
Dipartimento di Architettura, Design e Urbanistica, Università degli Studi di Sassari, Alghero, Italy

BERNARDINO CHIAIA: `bernardino.chiaia@polito.it`
Dipartimento di Ingegneria Strutturale, Edile e Geotecnica, Politecnico di Torino, Torino, Italy

ANIL MISRA: `anmisra@fiu.edu`
Florida International University, Miami, FL, United States

LUCA PLACIDI: `luca.placidi@unipegaso.it`
Department of Engineering, Telematic University Pegaso, Napoli, Italy